

Steady-State Parallel Retreat Migration in River Bends with Noncohesive 1 (Composite) Banks

David Waterman¹ and Marcelo Garcia²

¹South Dakota School of Mines and Technology

²University of Illinois

November 22, 2022

Abstract

A substantial body of research has addressed the equilibrium cross-sectional geometry of straight noncohesive channels, along with bends having fixed outer banks. However, development of a characteristic cross-section during active migration has been confounded by inaccurate treatment of noncohesive bank erosion processes. This analysis characterizes a steady-state migrating cross-section and the associated migration rate for the highly conceptualized case of an infinite bend of constant centerline radius with noncohesive lower banks consisting of uniform-sized grains mobilized as bedload. Analytical, numerical, and field analyses are presented to rationally constrain the geometry and obtain a physically based migration rate equation dependent on the following dimensionless groupings: excess Shields stress, flow depth to radius of curvature ratio, and noncohesive bank thickness to grain size ratio. Migration rate is shown to be dictated by transverse sediment flux at the thalweg due to secondary flow, not bank slope as in previous formulations developed from similar principles. Simple outward translation can result without the characteristic cyclic process observed in cohesive banks (fluvial erosion, oversteepening, and mass failure). This suggests that the linear excess shear stress formulation that applies to cohesive soils misrepresents noncohesive bank erosion processes. A numerical model of cross-sectional evolution to steady-state migration is developed; when applied to the lower Mackinaw River in Illinois, it reveals that the river behaves as if the critical shear stress is considerably larger than that indicated by the grain size distribution. This conceptualized treatment is intended to provide a canonical basis of comparison for actual meander bend geometries.

17 **Abstract**

18 A substantial body of research has addressed the equilibrium cross-sectional geometry of straight
19 noncohesive channels, along with bends having fixed outer banks. However, development of a
20 characteristic cross-section during active migration has been confounded by inaccurate treatment
21 of noncohesive bank erosion processes. This analysis characterizes a steady-state migrating
22 cross-section and the associated migration rate for the highly conceptualized case of an infinite
23 bend of constant centerline radius with noncohesive lower banks consisting of uniform-sized
24 grains mobilized as bedload. Analytical, numerical, and field analyses are presented to rationally
25 constrain the geometry and obtain a physically based migration rate equation dependent on the
26 following dimensionless groupings: excess Shields stress, flow depth to radius of curvature ratio,
27 and noncohesive bank thickness to grain size ratio. Migration rate is shown to be dictated by
28 transverse sediment flux at the thalweg due to secondary flow, not bank slope as in previous
29 formulations developed from similar principles. Simple outward translation can result without
30 the characteristic cyclic process observed in cohesive banks (fluvial erosion, oversteepening, and
31 mass failure). This suggests that the linear excess shear stress formulation that applies to
32 cohesive soils misrepresents noncohesive bank erosion processes. A numerical model of cross-
33 sectional evolution to steady-state migration is developed; when applied to the lower Mackinaw
34 River in Illinois, it reveals that the river behaves as if the critical shear stress is considerably
35 larger than that indicated by the grain size distribution. This conceptualized treatment is intended
36 to provide a canonical basis of comparison for actual meander bend geometries.

37 **Plain Language Summary**

38 Meandering rivers erode their outer banks and deposit coarse-grained sand and gravel on the
39 inside of bends. Finer-grained sediments (fine sand, silt, clay) deposit on top of the coarse-
40 grained bar deposits. The fine-grained sediments generally are more cohesive and have increased
41 strength and resistance to erosion. As the river migrates back and forth across its floodplain, the
42 outer bank is commonly eroding into a bar deposit left behind by a former river configuration.
43 This type of bank with a lower layer of sand and gravel and an upper layer of cohesive soil is
44 known as a composite riverbank. River engineers need to predict migration rates to determine
45 risk to infrastructure and to design measures to mitigate such risks. The equation used to model
46 erosion of cohesive soils is mathematically simple. Largely because of the simplicity of the

47 cohesive sediment erosion rate equation, it has been used extensively to model the erosion of
48 coarse-grained sand and gravel banks, even though the dominant physical factors governing the
49 erosion are quite different than for cohesive soils. In this study, the characteristic shape and
50 migration rate of a river with noncohesive banks is sought, using physical principles of
51 sand/gravel erosion and deposition rather than the simplistic forms used for cohesive soils. A
52 migration rate formulation is developed, and key aspects of the river cross-sectional shape are
53 determined for an idealized case of a river bend migrating at steady state.

54 **1 Introduction**

55 1.1 Noncohesive bank deformation: state of the science summary

56 Bank soil composition is a primary factor that determines channel migration rates. Although few
57 natural channels have banks consisting entirely of coarse-grained, noncohesive soil, a composite
58 riverbank (Thorne & Tovey, 1981) is a common stratigraphy. A composite bank consists of a
59 lower layer of noncohesive soil overlain by an upper layer of fine sand, silt, and clay. In the
60 context of single-threaded meandering alluvial rivers, the lower layer is dominated by bed
61 material sized sediment originally emplaced as lateral accretion deposits during migration of the
62 stream across its floodplain. The upper layer consists of sediments primarily transported in
63 suspension and deposited on bar tops and overbank areas, aided by vegetation establishment
64 (e.g., Nanson, 1980; Tsujimoto, 1999). The primary mechanisms governing the erosion of
65 composite riverbanks are fluvial erosion of the noncohesive basal material and associated
66 geotechnical mass failure of the overlying material (Thorne & Tovey, 1981; Thorne, 1982). In
67 the past several decades, these processes have been incorporated into a multitude of bank erosion
68 models of varying sophistication; descriptions of relevant physical processes and many of the
69 modeling approaches can be found in Rinaldi and Darby (2008) and Klavon et al. (2017).

70 Properly characterizing the fluvial erosion of noncohesive bank materials remains a weakness of
71 morphodynamics models. This weakness exists despite substantial attention being given to the
72 topic of noncohesive bank deformation during the 1980s and 1990s (e.g., Ikeda, 1981; Ikeda et
73 al., 1988; Diplas, 1990; Pizzuto, 1990; Kovacs & Parker, 1994; Thorne et al., 1998). These
74 studies characterized evolution of banks to a threshold channel configuration when a straight
75 channel is subjected to excess boundary shear stress with the bank material mobilized as

76 bedload. The threshold channel concept (Glover & Florey, 1951), as modified by Parker (1978)
77 to account for an active bedload transporting region, provided a coherent framework upon which
78 bank deformation results could be generalized. Those studies that incorporated numerical
79 modeling implemented several approaches to account for momentum extraction due to the
80 transverse boundary layer associated with the bank; the resulting boundary shear stress
81 distribution was then used to drive the boundary deformation due to transverse bedload flux
82 divergence terms in the sediment mass conservation equation (Exner equation). Despite the
83 success of these early modeling approaches, implementation of the numerical techniques
84 developed for straight channels has been slow to be implemented into morphodynamics models
85 for natural channels. This can be attributed primarily to the increased complexity of natural
86 channel alignments and the consequent increased computational expense of accurately
87 characterizing boundary shear stresses at a suitable spatial resolution, an issue highlighted by
88 Rinaldi and Nardi (2013).

89 Presently, the most commonly used reach-scale modeling techniques that address fluvial erosion
90 of basal noncohesive bank materials can generally be classified into two broad categories, which
91 depend on the bank erosion modeling framework: (a) models that treat bank erosion through
92 analysis of individual cross sections, in which the boundary shape and boundary shear stress
93 distribution can be discretized at a denser spatial resolution than the width of the entire bank; and
94 (b) spatially continuous two-dimensional (2D) morphodynamics models, in which the entire
95 width of the bank at any longitudinal position along the stream may be comprised by few (or
96 one) numerical cells.

97 With respect to the first category of bank erosion models, the most common method for fluvial
98 erosion specifies the local fluvial erosion rate in the direction normal to the surface, E , as a linear
99 function of the excess boundary shear stress:

$$100 \quad E = k(|\boldsymbol{\tau}_b| - \tau_c) \quad (1)$$

101 where k is an erodibility coefficient, $\boldsymbol{\tau}_b$ is the boundary shear stress vector, and τ_c is the critical
102 boundary shear stress. This linear formulation is also known as the Ariathurai-Partheniades
103 equation (Ariathurai, 1974; McAnally & Mehta, 2001). The linear excess shear stress method is
104 used in models such as BSTEM (Simon et al., 2000), CONCEPTS (Langendoen & Simon,

105 2008), and various physics-based models developed for academic research (e.g., Darby et al.,
106 2007; Rinaldi et al., 2008). However, the formulation was developed based on experimental
107 results using cohesive sediments. A recognized knowledge gap has been identified regarding
108 suitable ways to specify the erodibility coefficient for noncohesive bank materials (e.g., Rinaldi
109 et al., 2008; Rinaldi & Nardi, 2013). Rinaldi and Darby (2008) were compelled to assume that
110 the equation is robust, given the lack of a suitable alternative, but they acknowledge that the
111 physical basis of the equation is questionable. Waterman and García (2016) described how Eq.
112 (1) is an entrainment rate equation that applies to sediments transported at less than the transport
113 capacity of the flow, which improperly characterizes sediment mass conservation when
114 dominated by noncohesive sediment transport. Nevertheless, the excess shear stress formulation
115 continues to be extensively used in the cross-sectional models, primarily due to its ease of
116 numerical implementation and long history of usage.

117 With respect to the second category of models, in which the bank region is discretized with few
118 numerical cells, simplified conceptualizations of fluvial erosion and mass failure are generally
119 “lumped” into algorithms of varying physical realism (Stecca et al., 2017). This lumped (or bulk)
120 treatment is a practical necessity due to computational limitations with respect to modeling
121 reach-scale spatially continuous domains. With this limitation in mind, the accurate expression of
122 sub-grid scale bank processes as net bank retreat remains one of the major challenges of modern
123 morphodynamics modeling (Siviglia & Crosato, 2016). The simplest of these lumped bank
124 erosion models, which are not specific to either cohesive or noncohesive banks, specify the bulk
125 bank retreat rate as a linear function of either the excess near-bank velocity or the excess near-
126 bank boundary shear stress. Excess velocity refers to the difference between the near-bank
127 velocity and the cross-sectional average velocity (Ikeda et al., 1981), while the excess shear
128 stress refers to the difference between the boundary shear stress and a critical shear stress
129 associated with the specific bank material. Mosselman (1998) explains that bulk bank erosion
130 models based on excess shear stress conceptually represent a time-averaged description of
131 parallel retreat (Osman and Thorne, 1988) that involves a cyclical sequence of basal fluvial
132 erosion followed by large-scale mass failure. Numerous lumped noncohesive bank erosion
133 algorithms of greater complexity are used in 2D morphodynamics models; the reader is referred
134 to Stecca et al. (2017) for an enumeration and analysis of the most common ones.

135 One type of lumped algorithm not addressed in Stecca et al. (2017) is the integral treatment of
136 the Exner equation applied over the bank region, which extends from the top of bank down to the
137 thalweg, as originally formulated by Hasegawa (1989). Presumably, that method was not
138 addressed in Stecca et al. (2017) because it is not widely used in 2D morphodynamics models.
139 However, the bank-integrated method provides a theoretically sound basis for treating
140 noncohesive soils. Hasegawa (1989) noted that the integral treatment mathematically formalized
141 bank retreat principles described by Thorne (1982), in which the bank migration rate is driven by
142 the balance between the supply of sediment from the bank to its base and the removal of that
143 material, resulting in parallel retreat under conditions of unimpeded removal. The approach of
144 Hasegawa (1989) was not exploited to its full advantage until more recently. Parker et al. (2011)
145 described the mathematics of the integral treatment in greater detail and noted that simplified
146 treatments yielding similar formulations were obtained and utilized by Duan et al. (2001) and
147 Duan and Julien (2005). Since the work of Parker et al. (2011), the bank-integrated approach has
148 been utilized by Asahi et al. (2013) and Eke et al. (2014), among others. The bank-integrated
149 Exner equation is further explored in this paper as a robust physics-based method to treat fluvial
150 erosion of noncohesive bank materials in bulk bank erosion models.

151 1.2 Motivation, Objectives, and Approach

152 Substantial research on composite riverbank migration in recent years has focused on channel
153 migration rates being influenced by differential rates of outer bank erosion and inner bank
154 accretion (e.g., Parker et al., 2011; Eke et al., 2014) and on slump block armoring of the
155 noncohesive bank layer (e.g., Parker et al., 2011; Motta et al., 2014; Hackney et al., 2015).
156 However, more fundamental questions remain unanswered. For example, if the inner bank and
157 outer bank were to migrate at equal rates (constant-width migration), what would be the expected
158 cross-sectional shape of the channel, particularly in the bank region? Similarly, if bank armoring
159 were not present, what would be the bank shape and the migration rate? The present analysis is
160 motivated by these questions, with the intention that the answers will both improve fundamental
161 understanding of noncohesive bank migration and yield useful results for modeling.

162 The bank-integrated Exner equation approach for bank migration requires calculation of the
163 transverse flux of sediment from the base of the bank region, which is dependent on both the

164 effects of secondary flow and gravity due to bank slope on bedload movement. The integral
165 treatment as implemented by Hasegawa (1989) and Parker et al. (2011) requires a similarity
166 function for the cross-sectional shape of the bank. In those analyses, the bank shape was assumed
167 to have a uniform transverse slope; however, a rational physically-based manner of specifying
168 the bank shape *a priori* has never been established. Thus, the first objective of the analysis is to
169 suitably constrain the bank shape for use in the integral treatment. The second objective is to
170 utilize the shape constraint to express the bank-integrated Exner equation for migration rate in a
171 suitable form for implementation in numerical models of rivers having noncohesive or composite
172 banks. The third objective is to demonstrate numerically that parallel retreat as conceived in the
173 analytical treatment as a simple outward translation of the cross-section (not the cyclic process of
174 fluvial erosion, oversteepening, and mass failure) is feasible in noncohesive bank materials.

175 Simplification is required to satisfy the objectives and elucidate the essential aspects of
176 noncohesive bank deformation in meandering rivers. The following simplifications are
177 implemented in the current analysis: (a) fully-developed flow in a constant radius bend of low to
178 moderate curvature based on the nomenclature of Blanckaert (2011); (b) uniform-sized sediment
179 mobilized only as bedload; (c) the fine-grained upper layer plays no role in the bank migration
180 dynamics, e.g., through armoring of the noncohesive layer. The cross-sectional shape is sought
181 that migrates without changing shape (parallel retreat) under a constant discharge. The simplified
182 analysis indicates a tendency toward which channel geometry can be expected to adjust for a
183 given discharge and provides the canonical case for evaluating deviations from the idealized
184 conditions. More physically realistic representations of all the complexities of natural channels
185 can be developed in the future once the simplest condition is better understood.

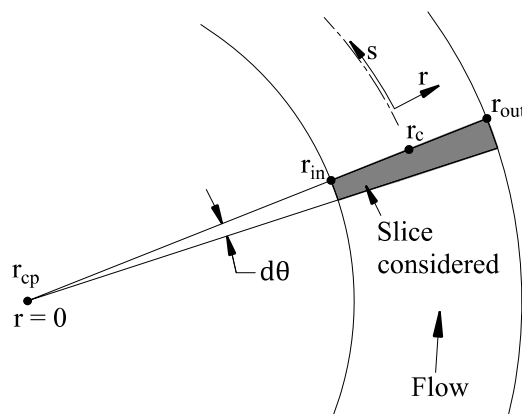
186 The paper is organized as follows. In Section 2, the integrated Exner equation is explored to
187 identify the conditions required to achieve parallel retreat and to establish the basic form of the
188 migration rate equation whose terms must be quantified. Section 3 theoretically establishes the
189 parallel retreat shape constraint of zero transverse slope (horizontal) at the channel thalweg; this
190 is contrasted with the implied similarity functions of Hasegawa (1989) and Parker et al. (2011).
191 The new shape constraint allows further quantification of terms in the migration rate equation,
192 which is then expressed in dimensionless form as a function of the excess Shields stress. In
193 Section 4, a simplified numerical model is presented to demonstrate that parallel retreat as simple

194 translation is feasible in noncohesive materials as conceived in the theoretical analysis. In
 195 Section 5, the numerical model is applied to a bend of the Mackinaw River, and the simulation
 196 parameters that yield results that best represent the field observations are described. Finally, in
 197 Section 6 organizing principles are discussed that provide a coherent framework upon which
 198 noncohesive bank deformation can be generalized across both straight and meandering reaches;
 199 the results are also discussed in terms of relating the highly simplified conceptual model to the
 200 complexities of real rivers.

201 **2 Mathematical and Physical Bases of Parallel Retreat**

202 **2.1 Integrated Exner Equation and Assumptions**

203 The infinite bend configuration (fully-developed flow, constant centerline radius) used
 204 throughout this analysis is illustrated in Figure 1. The governing equations are most conveniently
 205 expressed in modified cylindrical coordinates (s, r, z), where s is the streamwise coordinate, r is
 206 the radial coordinate, and z is the vertical coordinate. The modified cylindrical coordinates are
 207 converted to standard cylindrical coordinates based on the relationship $s = r\theta$, where θ is the
 208 angle turned about the center point in a plane where $z = \text{constant}$. The longitudinal slope of the
 209 channel is considered small, such that (s, r, z) are orthogonal coordinates. The variables r_{in} , r_c ,
 210 and r_{out} represent the radii of the inner boundary, the centerline, and the outer boundary of the
 211 channel, respectively. The radial position of the center point of the circle is denoted r_{cp} , which
 212 always equals 0.

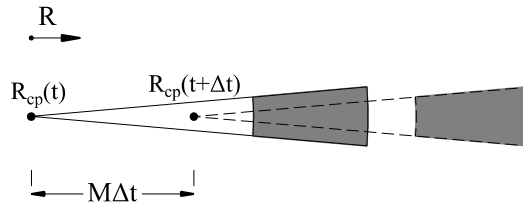


213

214

Figure 1: Plan view showing radial slice considered in analysis

215 The constant migration rate M is sought for a channel geometry that does not change during
 216 migration under a steady bankfull discharge Q_{bf} . To maintain constant radial values as the
 217 channel migrates, the (s, r, z) coordinate system must represent a translating frame of reference
 218 rather than concentric expansion on a fixed frame of reference. The resulting governing
 219 equations have the same basic structure as the more commonly used intrinsic (s, n, z) coordinate
 220 system (e.g., Parker et al., 2011) where the origin of the transverse n coordinate is associated
 221 with the dynamic channel centerline. In Figure 2, the translating frame of reference is illustrated
 222 with respect to a fixed frame of reference, in which the radial coordinate for the latter is denoted
 223 with R . For each value r_{cp} , r_{in} , r_c , and r_{out} in the translating system, an associated value R_{cp} , R_{in} ,
 224 R_c , and R_{out} , respectively, exists in the fixed frame of reference.



225

226 **Figure 2:** Plan view showing translated radial slice on a fixed coordinate system after a long time interval Δt

227 In Fig. 2, the shaded region represents the channel and t represents time. The following relations
 228 describe the time-invariant radial quantities under the constant migration rate M .

229
$$\frac{dr_{in}}{dt} = \frac{dr_c}{dt} = \frac{dr_{out}}{dt} = 0 \quad (2)$$

230
$$\frac{\partial r_{in}}{\partial t} = \frac{\partial r_c}{\partial t} = \frac{\partial r_{out}}{\partial t} = M \quad (3)$$

231 The above relations are ensured through evaluating the total derivative, with the following
 232 expressions being valid for any of the r terms:

233
$$r = R - R_{cp} \quad (4)$$

234
$$\frac{dr}{dt} = \frac{\partial r}{\partial t} + \frac{\partial r}{\partial R_{cp}} \frac{dR_{cp}}{dt} \quad (5)$$

235 where dR_{cp}/dt is the migration rate M and $\partial r/\partial R_{cp}$ is -1 from Eq. (4). The constant channel width
 236 B is expressed as $B = r_{out} - r_{in}$. The steady discharge Q_{bf} is entirely conveyed between r_{in} and r_{out} .

237 The volumetric bedload transport rate per unit width vector, \mathbf{q} , is decomposed into a streamwise
 238 component, q_s , and a transverse component tangent to the boundary surface in the r - z plane, q_{rt} .
 239 In modified cylindrical coordinates, the Exner equation is expressed as:

$$240 \quad \frac{\partial \eta}{\partial t} = -\frac{1}{(1-\lambda)} \left[\frac{\partial q_s}{\partial s} + \frac{\partial q_{rt}}{\partial r} + \frac{q_{rt}}{r} \right] \quad (6)$$

241 where η represents the surface elevation above an arbitrary vertical datum, and λ is the porosity
 242 of the granular medium. The partial derivative of q_{rt} is taken with respect to the coordinate r
 243 rather than a boundary-fitted coordinate defined tangent to the surface in the r - z plane, as derived
 244 in Waterman and García (2016). In steady, uniform bend flow, the divergence terms in the s -
 245 direction vanish, allowing simplification to:

$$246 \quad \frac{\partial \eta}{\partial t} = -\frac{1}{(1-\lambda)} \left[\frac{\partial q_{rt}}{\partial r} + \frac{q_{rt}}{r} \right] \quad (7)$$

247 Utilizing the definition of the total derivative of $\eta(t, r)$ yields the following:

$$248 \quad \frac{d\eta}{dt} = \frac{\partial \eta}{\partial t} + \frac{\partial \eta}{\partial r} \frac{\partial r}{\partial t} \quad (8)$$

249 For parallel migration, in which the shape does not change within the translating frame of
 250 reference, $d\eta/dt = 0$. This treatment presupposes that the parallel retreat process is not a time-
 251 averaged depiction of a cyclical process of basal erosion and mass failure in the bank region, but
 252 rather a simple translation of the entire cross section due to local erosion and deposition.

253 Substituting from Eq. (3), Eq. (8) is re-expressed accordingly:

$$254 \quad \frac{\partial \eta}{\partial t} = -M \frac{\partial \eta}{\partial r} \quad (9)$$

255 Eq. (9) ensures that the bank region is erosional when considered on a fixed frame of reference
 256 due to $\partial \eta / \partial r$ being positive. Substituting Eq. (9) into Eq. (7) yields:

$$257 \quad M(1-\lambda) \frac{\partial \eta}{\partial r} = \frac{\partial q_{rt}}{\partial r} + \frac{q_{rt}}{r} \quad (10)$$

258 Following the technique of Hasegawa (1989) and Parker et al. (2011), Eq. (10) is integrated in
 259 the radial direction; the limits of integration can be set at any arbitrary r positions on the cross-
 260 section. Integrating over the r -direction between arbitrary radial positions r_A and r_B yields:

$$261 \quad M(1 - \lambda)(\eta|_{r_B} - \eta|_{r_A}) = q_{rt}|_{r_B} - q_{rt}|_{r_A} + \int_{r_A}^{r_B} \frac{q_{rt}}{r} dr \quad (11)$$

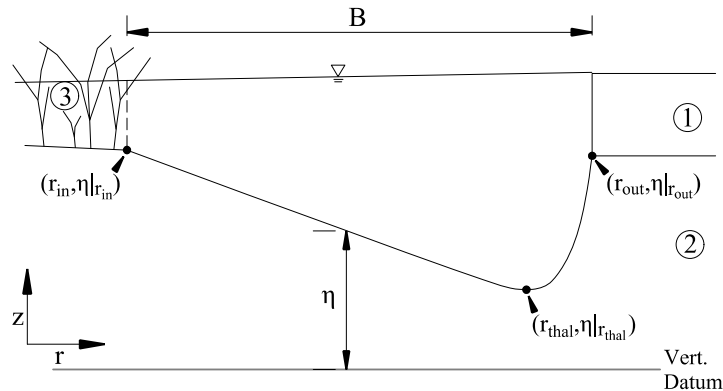
$$262 \quad M = \frac{q_{rt}|_{r_B} - q_{rt}|_{r_A} + \int_{r_A}^{r_B} \frac{q_{rt}}{r} dr}{(1 - \lambda)(\eta|_{r_B} - \eta|_{r_A})} \quad (12)$$

263 Note that the same result is obtained by integrating Eq. (7) over the r direction and implementing
 264 the Leibniz integral rule, which was the technique used by Parker et al. (2011). Ultimately, Eq.
 265 (12) will be used to formulate the migration rate; a key aspect of the analysis is to appropriately
 266 establish the positions r_A and r_B where q_{rt} and η can be readily quantified.

267 2.2 Boundary Conditions and their Implications

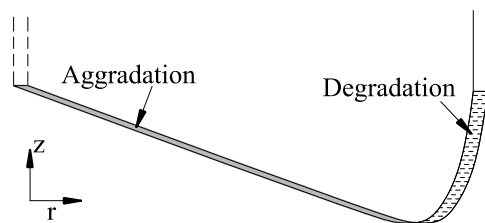
268 The boundary condition is imposed that $q_{rt}|_{r_{out}} = 0$; i.e., no bedload enters the domain from the
 269 cohesive upper layer as the channel migrates. Under the idealized condition, the upper cohesive
 270 layer passively fails as the noncohesive layer migrates, and that material is carried away in
 271 suspension. The boundary condition is also imposed that $q_{rt}|_{r_{in}} = 0$. The basis of the latter
 272 boundary condition is that, by problem definition, no discharge is conveyed where $r < r_{in}$. Thus,
 273 the mean flow velocity, bed shear stress, and bedload transport rate at the boundary are equal to
 274 zero. The conceptual interface at $r = r_{in}$ is illustrated in Fig. 3; the flow depth is non-zero at the
 275 interface, but dense vegetation in the region $r < r_{in}$ is presumed to maintain negligible velocity.
 276 The necessity of the non-zero flow depth at the inner boundary is described later in this section.
 277 The circled numbers in Fig. 3 indicate the following characteristics of the regions that form the
 278 channel boundary and just beyond it: (1) cohesive upper layer; (2) noncohesive lower layer; (3)
 279 vegetated over-bar area that is submerged under moderate and high flow conditions. Fig. 3 shows
 280 that $\eta|_{r_{in}}$ and $\eta|_{r_{out}}$ are elevations associated with the noncohesive layer and r_{thal} is the radial
 281 coordinate of the thalweg. Fig. 4 illustrates regions of aggradation (net deposition) and
 282 degradation (net erosion) that must exist in a fixed spatial frame of reference under conditions of
 283 parallel retreat. The shape of the cross-section in Figs. 3 and 4 is not imposed; the only shape
 284 assumption made is that $\partial\eta/\partial r \leq 0$ throughout the region left of the thalweg and $\partial\eta/\partial r \geq 0$

285 throughout the region right of the thalweg. The cross-sectional shape illustrated in the figures is
 286 only provided to aid the description of the problem setup.



287
 288

Figure 3: Cross-sectional view showing radial slice considered in analysis



289
 290
 291

Figure 4: Cross-sectional view showing the translating section on a fixed spatial frame of reference at two instants in time

292 With the shape assumption that $\partial\eta/\partial r \leq 0$ throughout the region left of the thalweg, the outermost
 293 location of maximum η must be aggradational and emplaced as the channel migrates. Since
 294 aggradation necessitates the condition that $\partial q_{rt}/\partial r \neq 0$, the flow must be competent to transport
 295 bedload infinitesimally close to the location of maximum η . This establishes the non-zero flow
 296 depth requirement at the inner boundary illustrated in Fig. 3.

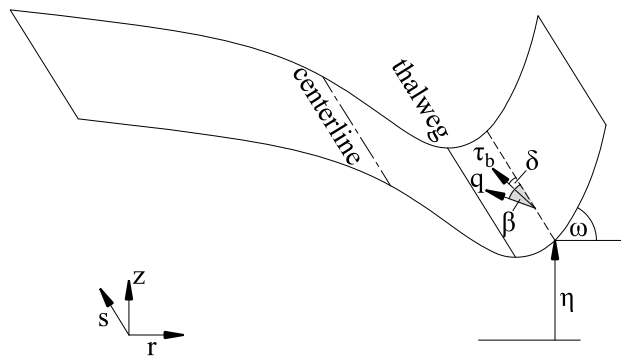
297 The $q_{rt}|_{r_{out}} = q_{rt}|_{r_{in}} = 0$ boundary conditions also have implications on the elevation of $\eta|_{r_{in}}$ relative
 298 to $\eta|_{r_{out}}$. To achieve parallel migration, the volume of noncohesive sediment eroded must be
 299 exactly balanced by the volume deposited in the fixed frame of reference. However, the eroded
 300 sediment originates from the region where a control volume has a relatively large dimension in
 301 the s -direction, while sediment deposits in the region where a control volume has a smaller s -
 302 direction dimension (see Fig. 1). Thus, to achieve the volume balance, deposited sediment must
 303 reach a somewhat higher elevation at the inner edge than the elevation of eroded material at the
 304 outer edge to compensate for the control volume shape. The mathematical demonstration of this

305 assertion is provided in Appendix A. This requires that $\eta|_{r_{out}}$ cannot be arbitrarily high on the
 306 outer bank but must be lower than the elevation at which bedload can be transported at the inner
 307 bank.

308 3 Rational Shape Constraint and Resulting Migration Rate Equation

309 3.1 Development of the Shape Constraint

310 The key to using Eq. (12) is appropriately establishing the positions r_A and r_B where q_{rt} and η can
 311 be readily quantified. At the outer boundary, $q_{rt} = 0$, and $\eta|_{r_{out}}$ can be estimated with respect to the
 312 top of bank using a typical depth of the cohesive top layer. Therefore, r_{out} is the most straight-
 313 forward choice for setting r_B in Eq. (12). Selecting the position r_A is more challenging, as q_{rt} is a
 314 function of the covarying hydrodynamics and boundary shape, which are not known *a priori*. A
 315 rational shape constraint to generalize the calculation of q_{rt} at a specific location r_A is therefore
 316 sought. Figure 5 is a definition diagram showing variables required for the bedload transport rate
 317 evaluation, and previously undefined variables shown are described after the figure.



318
 319 **Figure 5:** Oblique view of channel illustrating several angles used in the bedload transport calculations

320 On Fig. 5, the variable δ is the deviation angle of τ_b relative to the s -direction, with the positive
 321 direction always toward the outer bank; β is the deviation angle of q relative to the s -direction,
 322 with the positive direction always toward the outer bank; and ω is the boundary inclination
 323 angle, defined according to:

$$324 \quad \tan \omega = \frac{\partial \eta}{\partial r} \quad (13)$$

325 The calculation of q_{rt} requires Eqs. (14) through (20):

$$326 \quad \tau_c = K_B \tau_{c0} \quad (14)$$

$$327 \quad K_B = \frac{\sin \omega \sin \delta}{\mu_s} + \sqrt{\left(\frac{\sin \omega \sin \delta}{\mu_s}\right)^2 - \left(\frac{\sin \omega}{\mu_s}\right)^2 + \cos^2 \omega} \quad (15)$$

$$328 \quad \mu_s = \tan \theta_{rp} \quad (16)$$

329 where K_B is the dimensionless Brooks coefficient (Brooks & Shukry, 1963); τ_{c0} is the critical
 330 shear stress on a horizontal bed; μ_s is the static friction coefficient; and θ_{rp} is the particle angle of
 331 repose (Wiberg and Smith, 1987). A summary of the derivation of K_B is provided in Vanoni
 332 (1975). When using the assumption of transverse slope only (longitudinal slope negligible), the
 333 relation of Kovacs and Parker (1994; Eq. 18 therein) is identical to the above formulation. When
 334 $\delta = 0$, K_B is equivalent to the more commonly known expression from Lane (1955; Eq. 1
 335 therein). The bedload transport rate vector magnitude is calculated according to:

$$336 \quad |\mathbf{q}^*| \equiv \frac{|\mathbf{q}|}{\sqrt{gR_s D_{50} D_{50}}} = \begin{cases} K_0 (|\boldsymbol{\tau}^*| - \tau_c^*)^{1.5} & \text{for } |\boldsymbol{\tau}^*| > \tau_c^* \\ 0 & \text{for } |\boldsymbol{\tau}^*| \leq \tau_c^* \end{cases} \quad (17)$$

$$337 \quad \boldsymbol{\tau}^* \equiv \frac{\boldsymbol{\tau}_b}{\rho g R_s D_{50}} \quad (18)$$

338 where \mathbf{q}^* is the dimensionless volumetric bedload transport rate per unit width; g is the
 339 gravitational acceleration constant; R_s is the sediment submerged specific gravity; D_{50} is the
 340 median sediment grain size, which in the present analysis is the specified uniform grain size; K_0
 341 is an empirical constant, which equals 5.7 in Fernandez-Luque and van Beek (1976); $\boldsymbol{\tau}^*$ is the
 342 Shields number; and τ_c^* is τ_c made dimensionless using Eq. (18). The bedload transport rate
 343 vector direction is calculated according to:

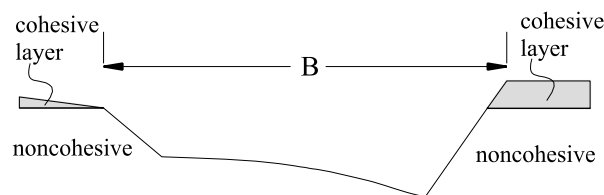
$$344 \quad \tan \beta \equiv \frac{q_{rt}}{q_s} = \tan \delta - A \left(\frac{\tau_{c0}^*}{|\boldsymbol{\tau}^*|} \right)^{0.5} \tan \omega \quad (19)$$

345 where A is a coefficient that is assumed constant in linear formulations (e.g., Parker, 1984) and
 346 has dependence on β , ω and δ in nonlinear formulations that account for steep slopes (Waterman
 347 & García, 2019). Following calculation of $|\mathbf{q}^*|$ and β , q_{rt} is calculated as:

$$348 \quad q_{rt} = |\mathbf{q}^*| \sqrt{gR_s D_{50} D_{50}} \sin \beta = |\mathbf{q}^*| \sqrt{gR_s D_{50} D_{50}} \frac{\tan \beta}{(1 + \tan^2 \beta)^{0.5}} \quad (20)$$

349 Direct calculation of q_{rt} is possible if values for τ_b (both magnitude and direction) and ω are
 350 known, which highlights the importance of being able to specify ω at the location where r_A will
 351 be chosen. In previous analyses, Hasegawa (1989) and Parker et al. (2011) specified ω as a
 352 constant value over the entire bank and set the position r_A for usage in their integral formulations
 353 to the thalweg position; i.e., the inner boundary of the bank region. The thalweg is the most
 354 logical location for r_A , as it is a nonarbitrary feature that can be identified on any cross-section.
 355 However, the value of ω should not be assigned arbitrarily, as it clearly influences q_{rt} , through
 356 both τ_c (Eqs. 14 and 15) and β (Eq. 19). Further reinforcing this point, Hasegawa (1989)
 357 considered the $\tan\omega$ term in Eq. (19) to be the primary driver in the decomposition of q ; more
 358 specifically, he neglected the $\tan\delta$ term in Eq. (19) as being of a lower order of magnitude than
 359 the $\tan\omega$ term. This analysis reexamines that assumption by analytically establishing the value of
 360 ω at the thalweg.

361 The characteristic cross-section of Parker et al. (2011; Fig. 10 therein) is provided as Fig. 6
 362 below, as that cross-section is directly contrasted with an alternative shape constraint developed
 363 for the thalweg in the present analysis. Note that the Parker et al. (2011) cross-section was
 364 specifically intended not to be a parallel retreat cross-section, as it allowed the region bankward
 365 of the thalweg and barward of the thalweg to adjust independently.



366

367 **Figure 6:** The characteristic cross-section of Parker et al. (2011; Fig. 10 therein)

368 As the thalweg is defined as the position of minimum η on the cross-section, $\partial\eta/\partial r$ would equal
 369 zero if the function of η versus r was a continuous, differentiable function; thus, ω would equal
 370 zero. However, it is not evident that η versus r is necessarily a continuous, differentiable
 371 function; the abrupt grade-break at the thalweg in the Parker et al. (2011) cross-section is the
 372 alternative. Two different conditions may prevail at a potential grade-break: first is that in which
 373 q_{rt} varies continuously and smoothly with respect to r ; second is that in which an abrupt
 374 discontinuity in the relationship between q_{rt} and r exists at the thalweg, referred to as a shock in

375 Parker et al. (2011). In the first scenario, an abrupt topographic break is not possible. Continuous
 376 variation of q_{rt} with respect to r requires that $q_{rt}|_{r_{thal}}$, calculated from both ω values bounding the
 377 thalweg, be equal. For clarity, these ω values are referred to as ω_{left} and ω_{right} . To ensure
 378 sediment is evacuated from the bank region for a migrating cross-section, this $q_{rt}|_{r_{thal}}$ value must
 379 be negative. Although ω may have multiple values at a point in space, as in the case of the grade-
 380 break, τ^* must be single-valued at a point in space on physical grounds. As helical flow causes τ^*
 381 to be directed inward (to the left, negative δ) at a bend, bedload left of the thalweg is driven
 382 upslope, and bedload right of the thalweg is driven downslope; intuitively, q_{rt} should be more
 383 negative when comparing any ω_{right} to ω_{left} , and this is indeed the case, based on the following
 384 considerations. Noting that $q_{rt}|_{r_{thal}}$ equals $|q|\sin\beta$, the transverse slope influences both $|q|$ and β .
 385 Right of the thalweg, an increase in inclination tends to increase $|q|$ through a decrease in τ^*_c
 386 (Eqs. 14 and 15); while an increase in inclination makes β more negative (Eq. 19). Thus, q_{rt}
 387 monotonically becomes more negative with increased inclination. Left of the thalweg, the
 388 situation is more complex. An increase in inclination causes β to become more positive (Eq. 19),
 389 but $|q|$ does not monotonically increase or decrease; Eqs. (14) and (15) indicate that with
 390 increased inclination τ^*_c initially increases to a maximum greater than τ^*_{c0} and then decreases.
 391 While a mathematically elegant solution was not obtained to demonstrate that $q_{rt}|_{r_{thal}}$ cannot be the
 392 same for different values of ω under the specific conditions evaluated, the following expression
 393 obtained from Eqs. (14) through (20) is used for the demonstration:

$$394 \quad \frac{[q_{rt}]_{left}}{[q_{rt}]_{right}} = \frac{[(|\tau^*| - K_B \tau^*_{c0})^{1.5} \tan \beta / (1 + \tan^2 \beta)^{0.5}]_{left}}{[(|\tau^*| - K_B \tau^*_{c0})^{1.5} \tan \beta / (1 + \tan^2 \beta)^{0.5}]_{right}} \quad (21)$$

395 The variables K_B and β are each a function of ω and δ , which are calculated from Eqs. (15) and
 396 (19), respectively; $|\tau^*|$ and δ are treated as parameters and are evaluated across a reasonable
 397 parameter space based on gravel-bed streams. The variable ω_{right} is set to 0, which yields the
 398 least negative value of $q_{rt}|_{r_{thal}}$ that can be obtained for ω_{right} . For each combination of $|\tau^*|$ and δ
 399 evaluated, ω_{left} is evaluated over the entire range from 0 to -40 degrees at 1-degree intervals to
 400 find the maximum value of the ratio; a ratio of 1 for any $\omega_{left} < 0$ indicates the grade-break is
 401 possible. The value of $|\tau^*|$ is varied from 0.046 to 0.20 in intervals of 0.002; and δ is varied from
 402 -1 to -45 degrees in 1-degree intervals. All combinations of these parameters are evaluated.
 403 Constants used in the analysis are $\mu_s = 0.84$; $A = 1.54$; $\tau^*_{c0} = 0.045$. The results reveal that the

404 maximum value of the ratio in Eq. (21) is uniformly 1.0 for all combinations, associated with
 405 $\omega_{left} = 0$. Therefore, any $\omega_{right} > 0$ (resulting in a more negative q_{rt}) will not yield a solution; and
 406 the only solution is:

$$407 \quad \omega_{left} = \omega_{right} = 0 \quad (22)$$

$$408 \quad \omega|_{r_{thal}} = 0 \quad (23)$$

409 In other words, the grade-break is not permissible for this first scenario that does not include a
 410 shock condition. A potential complicating factor to the above analysis is whether the parameter A
 411 in Eq. (21) is properly treated as a constant. For transverse slopes up to approximately 10°
 412 relative to horizontal, this linear assumption includes minimal error compared to a more robust
 413 nonlinear formulation of A , such as that derived in Waterman and García (2019), which was
 414 based on Kovacs and Parker (1994) and Seminara et al. (2002). The nonlinear expression of A in
 415 Waterman and García (2019) is the following:

$$416 \quad A = \chi \frac{1}{(\mu_S \mu_D)^{0.5}} \left(\frac{\cos \omega (1 + \tan^2 \delta)}{\cos \beta \left(1 + \left(\tan \beta + \frac{\tan \omega}{\mu_D \cos \beta} \right)^2 \right)^{0.5}} \right)^{0.5} \quad (24)$$

417 where χ is a dimensionless coefficient that expresses the ratio between the mean fluid velocity
 418 impinging on a static particle versus a particle moving in the bedload layer; and μ_D is the
 419 dynamic friction coefficient. Solving β in Eq. (19) iteratively using the expression from Eq. (24)
 420 for A , the same process of evaluating Eq. (21) over the same parameter space is repeated. The
 421 results are identical; the maximum value of the ratio is 1.0 across the entire space, associated
 422 with $\omega_{left} = 0$.

423 The second scenario in which the grade-break may exist is that associated with an abrupt
 424 discontinuity in the q_{rt} versus r relationship. Under this shock condition, the only constraints to
 425 $q_{rt}|_{r_{thal}}$ values associated ω_{left} and ω_{right} are that the two $q_{rt}|_{r_{thal}}$ be negative to ensure sediment
 426 evacuation from the bank region; and the integral condition (Eq. 12) must have the same solution
 427 for both the region bankward of the thalweg (in which $r_A = r_{thal}$ and $r_B = r_{out}$) and inward of the
 428 thalweg (in which $r_A = r_{in}$ and $r_B = r_{thal}$). With only these constraints, the potential presence of a

429 grade-break cannot be disproven mathematically. Nevertheless, through physical reasoning,
 430 some approximate conclusions can be drawn. The τ_b distribution in the vicinity of the grade-
 431 break is effectively that which exists at the corner of a trapezoidal channel. The τ_b increases
 432 bankward of such a corner for a short distance, reaching its maximum value a short distance up
 433 the bank (e.g., Thorne et al., 1998; Khodashenas & Paquier, 1999), depending on the corner
 434 angle. Without any consideration of the region interior to the thalweg, for such a situation to
 435 exist under parallel retreat, Eq. (9) requires that the outer bank must be erosional across its
 436 entirety; and Eq. (7) requires that $\partial q_{rl}/\partial r$ be positive over its entirety to counteract the effect of
 437 the negative q_{rl}/r and ensure erosion. However, in the near-corner region, q_{rl} would be more
 438 negative moving outward ($\partial q_{rl}/\partial r$ negative) where τ_b increases up a slope of constant or
 439 increasing ω . This violates the requirement of Eq. (9); during bank profile evolution, the near-
 440 corner region will be depositional according to Eq. (7), thus tending to smooth out the
 441 discontinuity. This always occurs in the development of straight channel experiments in uniform
 442 noncohesive materials (e.g., Ikeda, 1981), and also for the few documented cross-section sets in
 443 noncohesive experimental meandering channels (e.g., Friedkin, 1945; Schumm and Khan, 1972),
 444 even though these latter cannot be presumed to constitute equilibrium parallel retreat cross-
 445 sections. While this does not rise to the level of mathematical proof, it does suggest that the
 446 formation of a grade-break is unlikely under the assumptions of this analysis, and the most
 447 justifiable shape constraint is the one developed previously, namely that $\omega|_{r_{thal}} = 0$.

448 3.2 Migration Rate Equation

449 The migration rate formulation is preferably expressed in terms of either excess shear stress or
 450 excess velocity to maintain convention and provide a more direct comparison with past
 451 formulations. The $\omega|_{r_{thal}} = 0$ shape constraint has convenient consequences with respect to
 452 implementation in Eq. (12) when setting r_A to r_{thal} . First, according to Eqs. (14) and (15), $\tau_c = \tau_{c0}$.
 453 Second, according to Eq. (19), $\tan\beta = \tan\delta$. Third, with $\omega = 0$, simple formulations for the
 454 bedload transport vector magnitude (Eq. 17) contain no error associated with the effect of steep
 455 slopes. These three factors lead to simplifications in developing Eq. (12) into the form of an
 456 excess shear stress equation. Setting the positions $r_A = r_{thal}$ and $r_B = r_{out}$ in Eq. (12), with the
 457 boundary condition that $q_{rl}|_{r_{out}} = 0$, yields the following equation:

$$M = \frac{-q_{rt}|_{r_{thal}} + \int_{r_{thal}}^{r_{out}} \frac{q_{rt}}{r} dr}{(1-\lambda)(\eta|_{r_{out}} - \eta|_{r_{thal}})} \quad (25)$$

459 Since the shape constraint does not fully specify the channel geometry through a similarity
 460 function, various terms must be left in the formulation as parameters to be specified or neglected
 461 on order-of-magnitude considerations until future advances are achieved. Of primary concern are
 462 the following: (1) $\eta|_{r_{thal}}$; (2) the transverse proximity of r_{thal} to r_{out} , which determines the
 463 momentum extraction due to the side-wall effects, and consequently directly affects $q_{rt}|_{r_{thal}}$; and
 464 (3) the integral term in the numerator that results from the varying shape of the control volume in
 465 the radial direction. The latter term can be neglected on order-of-magnitude considerations,
 466 based on the following factors. At the thalweg, $\tan\beta = \tan\delta$ and the near-bed flow is toward the
 467 inside of the bend (e.g., Rozovskii, 1961); thus, $\tan\beta$, $\tan\delta$, and q_{rt} are negative at r_{thal} . This
 468 requires that q_{rt} transition from the negative value at r_{thal} to zero at r_{out} . Eq. (10) indicates that
 469 where $\partial\eta/\partial r=0$, then $\partial q_{rt}/\partial r \approx 0$; i.e., it is near a local minimum in q_{rt} versus r . When making the
 470 conservative assumption that the large negative q_{rt} value that prevails at the thalweg is constant
 471 over the integral limits, the integral is still smaller than the first term in the numerator by a factor
 472 of $\ln(r_{out}/r_{thal})$. This logarithm will generally be less than 0.1 ($r_{out}/r_{thal} < 1.1$), given that the width
 473 of the bank region is generally much smaller than the thalweg radius.

474 To further refine Eq. (25), q must be obtained through hydrodynamic analysis and then
 475 decomposed to express $q_{rt}|_{r_{thal}}$. For the case of steady, uniform bend flow, the s -momentum
 476 equation for a thin control volume encompassing the full flow depth can be expressed in the
 477 following alternative forms upon neglecting the cross-stream and vertical transport of s -
 478 momentum:

$$479 \quad \tau_{b,s} = c_0 \rho g h S \quad (26a)$$

$$480 \quad \tau_{b,s} = \rho g h' S \quad (26b)$$

481 where $\tau_{b,s}$ is the s -component of τ_b . Eq. (26a) is based on a thin control volume with vertical
 482 edges in which c_0 is a dimensionless coefficient between 0 and 1 (e.g., Ikeda & Nishimura, 1986)
 483 that accounts for momentum extraction due to fluid shear stress on the transverse face associated
 484 with the bank; h is the local flow depth; and S is the local longitudinal slope. Eq. (26b) is based

485 on an irregular-shaped control volume configured such that the s -directed fluid shear stresses on
 486 the transverse faces equal 0 (e.g., Pizzuto, 1990). In this configuration, h' is the local hydraulic
 487 radius, which is the cross-sectional area of the irregular control volume divided by its wetted
 488 perimeter. From Eqs. (26a) and (26b):

$$489 \quad h' \equiv c_0 h \quad (27)$$

490 The transverse component of τ_b for steady, uniform bend flow can be calculated based on the
 491 analytical treatments of van Bendegom (1947), Rozovskii (1961), and others, which take the
 492 form:

$$493 \quad \tan \delta \equiv \frac{\tau_{b,rt}}{\tau_{b,s}} = -K_1 \frac{h'}{r} = -K_1 c_0 \frac{h}{r} \quad (28)$$

494 where $\tau_{b,rt}$ is the transverse component of τ_b tangent to the plane of the surface; and K_1 is an order
 495 10 dimensionless constant taking values between 7 (Engelund, 1974) and 11 (Rozovskii, 1961).
 496 The theoretical analyses that established Eq. (28) were based on integration over a vertical slice
 497 of the stream unaffected by the fluid shear stress associated with the side walls. As a result, van
 498 Bendegom (1947) and Rozovskii (1961) obtained the local flow depth (h) rather than h' in the
 499 numerator of Eq. (28). However, when integrating the centripetal acceleration, the radial pressure
 500 gradient, and the boundary shear stress following van Bendegom (1947) over an irregular control
 501 volume configured to eliminate shear stress on the transverse faces, the variable that results is h' ,
 502 which is equivalent to h when the control volume is a vertical slice unaffected by side walls. The
 503 resultant boundary shear stress is used to calculate the bedload transport rate:

$$504 \quad |\tau_b| = \gamma \tau_{b,s} \quad (29)$$

$$505 \quad \gamma \equiv (1 + \tan^2 \delta)^{0.5} \quad (30)$$

506 where γ is defined to make subsequent equations more concise. The following conditions prevail
 507 at the thalweg: $\omega = 0$; $\tan \beta = \tan \delta$; and $\tau_c = \tau_{c,0}$. An expression for $q_{rt}|_{r_{thal}}$ is obtained using Eqs.
 508 (17) through (20) and Eq. (28):

$$509 \quad q_{rt}|_{r_{thal}} = \left(-\frac{c_0 K_0 K_1}{\gamma} (\gamma \tau_{b,s}^* - \tau_{c0}^*)^{1.5} \sqrt{g R_s D_{50} D_{50} \frac{h}{r}} \right) \Big|_{r_{thal}} \quad (31)$$

510 Note that if $\gamma = 1$ is specified, this is equivalent to the simpler, but less rigorous, approach of
 511 calculating q_s directly from $\tau_{b,s}$ rather than from $|\tau_b|$. Substituting Eq. (31) into Eq. (25) leads to a
 512 dimensionless migration rate equation that is in the form of an excess Shields stress formulation:

$$513 \quad M^* \equiv \frac{M}{\sqrt{gR_s D_{50}}} = \begin{cases} \left(\frac{c_0 K_0 K_1 D_{50} h}{\gamma(1-\lambda) H_{nc} r} (\gamma \tau_s^* - \tau_{c0}^*)^{1.5} \right) \Big|_{r_{thal}} & \text{for } \gamma \tau_s^* > \tau_{c0}^* \\ 0 & \text{for } \gamma \tau_s^* \leq \tau_{c0}^* \end{cases} \quad (32)$$

$$514 \quad H_{nc} \equiv (\eta|_{r_{out}} - \eta|_{r_{thal}}) \quad (33)$$

515 where M^* is the dimensionless migration rate; H_{nc} is the thickness of the noncohesive layer with
 516 respect to the deepest point in the channel; and τ_s^* is $\tau_{b,s}$ made dimensionless using Eq. (18).
 517 Although additional terms such as τ_s^* and γ can be more fully expressed in terms of h and r , the
 518 form of Eq. (32) is preferred, as it more directly expresses the migration rate dependence in
 519 terms of the following dimensionless groupings: (D_{50}/H_{nc}) , (h/r) , and τ_s^* . Note that when $h/r = 0$
 520 (straight channel), $M = 0$, as the steady state is simply the threshold channel that can contain a
 521 region of active bedload transport at the thalweg.

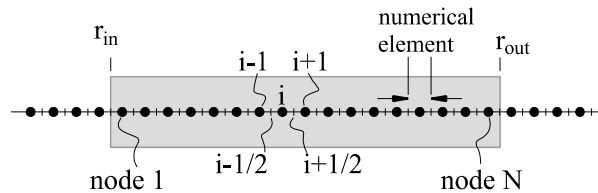
522 4 Numerical Model

523 4.1 Overview

524 A simplified numerical model is presented to answer several questions that the analytical
 525 treatment cannot: (1) Is parallel retreat possible without incorporating a time-averaged cyclical
 526 process of basal erosion and mass failure within the noncohesive layer? (2) What is the resulting
 527 channel shape ($\eta|_{r_{thal}}$, r_{thal} , etc.)? The first question naturally arises due to long-held
 528 misconceptions regarding the nature of fluvial erosion in noncohesive bank materials, which is
 529 rooted in the widespread usage of the linear excess shear stress formulation (Eq. 1) that strictly
 530 applies only to cohesive sediment. The second question arises due to various terms being needed
 531 in Eq. (32) that cannot be established without the channel shape (e.g., $\eta|_{r_{thal}}$ and c_0).

532 A cross-sectional numerical framework very similar to that developed by Stecca et al. (2017) is
 533 implemented herein. A 1-dimensional (1D, r -direction) fixed (Eulerian) grid is used, which is
 534 discretized into numerical elements at equal spacing Δr . The center of each numerical element is
 535 referred to as the node; calculated variables are nodal values. The constant-width region of

536 numerical elements comprising the active channel is numbered as nodes 1 through N. The active
 537 channel intermittently shifts outward in discrete single-node increments based on physical
 538 processes, which are discussed in Section 4.4. When the active channel region shifts, the nodes are
 539 renumbered 1 through N in the new active channel region, and radial coordinates are reassigned
 540 to the fixed numerical elements to maintain r_{in} , r_{out} , and r_c constant within the active channel
 541 region. An illustration of the 1D domain is provided in Figure 7.



542

543 **Figure 7:** Plan view showing 1D configuration of nodes (i , $i-1$, $i+1$) and boundaries of numerical elements ($i\pm 1/2$);
 544 the gray shading represents the active channel region of nodes that will shift rightward in time. A suitable spatial
 545 resolution is much denser than that shown; Δr is appropriately set to $<0.1 \times$ mean flow depth.

546 Quasi-steady, uniform, fully-developed bend flow is assumed, such that all divergence terms
 547 associated with mass and momentum fluxes in the s -direction are neglected. The parallel retreat
 548 cross-section under a specified bankfull discharge (Q_{bf}) is sought. Two required parameters are
 549 unknown: B and $\eta|_{r_{out}}$. The latter cannot be set arbitrarily high on the bank, as it potentially yields
 550 a condition in which more volume is eroded outside of the thalweg than can be deposited inside of
 551 the thalweg, thus preventing the development of steady-state migration. This issue is addressed in
 552 Appendix A, along with the rationale for establishing $\eta|_{r_{out}}$ as a function of B in Eq. (A12); therefore,
 553 only one unknown parameter B remains. The procedure is iterative, with an initial estimate of B
 554 and an arbitrary initial cross-sectional geometry specified. The numerical model contains two steps
 555 at each time interval, based on the quasi-steady approximation: (a) hydrodynamic calculation to
 556 obtain boundary shear stress distribution and subsequent calculation of q_{rt} ; and (b) boundary
 557 deformation based on an explicit finite difference representation of Eq. (7). For the hydrodynamic
 558 calculation, rather than solving the mass and momentum conservation equations for the given Q_{bf}
 559 by solving the water surface elevation, $\zeta(r)$, at each time step, an alternative procedure is used to
 560 reduce computation time. The transversely sloped water surface is maintained at the same
 561 elevations for nodes 1 through N throughout all time steps. The boundary shear stress distribution
 562 is calculated at each time step based on the momentum conservation equations. Q varies in time
 563 during the period of cross-section shape adjustment, since $\zeta(r)$ is time-invariant, whereas $\eta(r)$

564 varies in time. The hydrodynamic calculations are detailed in Section 4.2; the bedload transport
565 and boundary deformation calculations are detailed in Section 4.3.

566 The discrete time intervals between occurrences of active channel shifts defines ensembles of
567 changing channel geometry between shifts in the Eulerian framework; steady state is considered
568 to have been reached when cross-sectional geometries at specified times within ensembles have
569 elevation differences within a specified tolerance. The ensemble comparison technique is
570 described in Section 4.5. Once steady state is achieved, the calculated value of Q is evaluated with
571 respect to the solution condition $Q = Q_{bf}$. If the condition is satisfied, the solution is complete; if it
572 is not satisfied, then B is modified, and the procedure is repeated. The final solution is insensitive
573 to the initial cross-section, provided that some portion of the initial cross-section is deep enough
574 to yield $\tau_b > \tau_c$ at the bankfull flow level. All the parameters required for the model are provided
575 in a table in the model application of Section 5.

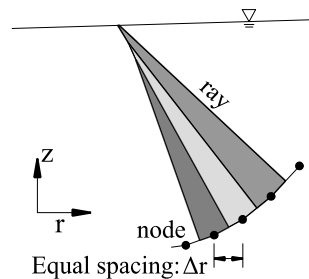
576 4.2 Hydrodynamic Treatment

577 The key requirement of the hydrodynamic model is to reasonably represent the boundary shear
578 stress distribution. The essence of the present treatment is the following assumptions: (a) the s -
579 momentum equation is dominated by the driving force due to gravity and the resisting force due
580 to fluid shear stresses; and (b) the r -momentum equation solution can be represented in an
581 approximate manner using simplified formulations for transverse water surface slope and the
582 deviation angle (δ) of the bed shear stress vector with respect to the s -direction. The momentum
583 equations, including those terms that are neglected in this treatment, are detailed in Appendix B.

584 The s -momentum treatment is described first. Neglecting terms such as the radial and vertical
585 transport of downstream momentum represents a somewhat crude approximation of the s -
586 momentum equation when treating the near-bank region in bend flow. However, the simplified
587 treatment that includes only gravity and boundary shear stress has proven to yield reasonably
588 accurate results in meandering river morphodynamics simulations focused on bank erosion
589 (Motta et al., 2014; Langendoen et al., 2016). The fluid shear stress on transverse faces of a
590 control volume is considered a potentially dominant term in the s -momentum equation,
591 particularly in the near-bank region. Therefore, control volumes are configured such that no s -
592 directed shear stresses exist on the transverse faces (e.g., Pizzuto, 1990), as opposed to

593 establishing control volumes configured vertically. The nonvertical control volumes used in the
 594 hydrodynamic treatment warrants the clarification that the nodal positions in the 1D domain (Fig.
 595 7) represent positions on the bottom boundary.

596 The specific method implemented to configure the control volumes with no fluid shear stresses
 597 on the transverse faces is the merged perpendicular method of Khodashenas and Paquier (1999),
 598 which is capable of treating concave-upwards, convex-upwards, and sharp-angled boundaries in
 599 the r - z plane. In this method, rays are extended upward-normal from the channel boundary until
 600 intersecting with the water surface or an adjacent ray. When two adjacent rays intersect, they are
 601 merged into a single ray segment beyond the intersection point; the merged segment is deflected
 602 intermediate to the orientations of the original rays. This yields a subdivision of the cross-section
 603 into adjacent nonoverlapping polygonal control volumes bounded by the rays. The rays originate
 604 from the bottom boundary at the lateral edges of each numerical element ($i \pm 1/2$; see Fig. 7). An
 605 illustration of the irregular control volumes based on this method are provided in Figure 8.



606

607 **Figure 8:** A conceptual illustration of three polygonal control volumes used to determine the boundary shear stress
 608 distribution in a small portion of the cross section. Note that polygons further to the left and right would alter the
 609 geometries of the three shown.

610 Rays are projected perpendicular to the boundary angle ω ; for the ray projection, $\omega_{i+1/2}$ is
 611 calculated as $\tan^{-1}((\eta_{i+3} - \eta_{i-2}) / (r_{i+3} - r_{i-2}))$, where the subscripts indicate the nodal position.
 612 Calculating $\omega_{i+1/2}$ in this manner effectively smooths the surface and is required to prevent
 613 numerical instability. The appropriate number of nodes to include in the smoothing decreases as
 614 the user-specified Δr value increases. Near nodes 1 and N, the number of nodes incorporated in
 615 the $\omega_{i+1/2}$ calculation is decreased to keep the smoothing window from extending beyond the
 616 limits of the active channel. Once the polygonal control volumes are geometrically defined, the
 617 local $\tau_{b,s}$ is calculated based on the force balance applied to the control volume. The downstream
 618 component of the water surface elevation gradient in fully developed bend flow is:

$$619 \quad S \equiv \frac{d\xi}{ds} = \frac{S_c r_c}{r} \quad (34)$$

620 where S_c is the longitudinal slope along the channel centerline. The s -dimension at the bottom
 621 boundary equals $r\Delta\theta$. The uniform Δr spacing yields wetted perimeters of the numerical control
 622 volumes equal to $\Delta r/\cos\omega$. For all the calculations following the ray projection, $\tan\omega_i$ is calculated
 623 using central differencing between nodes $i+1$ and $i-1$, except at nodes 1 and N , which are one-
 624 sided calculations. Balancing the gravitational driving force with the boundary shear force acting
 625 on a polygonal control volume yields the following:

$$626 \quad \tau_{b,s} = \rho g h' \frac{S_c r_c}{r} \quad (35)$$

$$627 \quad h' = \frac{A_i}{(\Delta r / \cos \omega)} \quad (36)$$

628 where A_i represents the cross-sectional area of the polygon in the r - z plane. An assumption of Eq.
 629 (35) is that the s -dimension and radial coordinate of the control volume are approximately constant
 630 over the entire height of the polygon, which is reasonable, provided that the ray length is small
 631 relative to r . Following calculation of $\tau_{b,s}$ for each numerical node, a boxcar smoothing procedure
 632 is implemented that averages the boundary shear stress at the numerical node with the three
 633 numerical nodes on each side of it. The smoothing procedure has the same effect as the approach
 634 recommended by Khodashenas and Paquier (1999) that involves reducing the number of numerical
 635 elements for the boundary shear stress calculation; however, the smoothing eliminates the need to
 636 subsequently reassign intermediate $\tau_{b,s}$ values to the more densely spaced numerical elements
 637 through a curve-fitting procedure. Otherwise, the numerical routine is exactly as outlined in
 638 Khodashenas and Paquier (1999). Following calculation of $\tau_{b,s}$, the polygon-averaged velocity (U_i)
 639 is calculated using a standard bed shear stress closure, followed by the total discharge:

$$640 \quad U_i = \left(\frac{\tau_{b,s}}{\rho C_f} \right)^{0.5} \quad (37)$$

$$641 \quad Q = \sum_{i=1}^N U_i A_i \quad (38)$$

642 where C_f is the dimensionless friction coefficient, which is treated as a constant parameter in this
 643 analysis.

644 With respect to the r component of momentum, the goal is to establish reasonable approximations
 645 of the transverse water surface slope and $\tau_{b,rt}$. The Jansen et al. (1979) analysis based on Rozovskii
 646 (1961) is used for the transverse water surface slope:

$$647 \quad \frac{d\xi}{dr} = \alpha_1 \frac{U^2}{rg} \quad (39)$$

$$648 \quad \alpha_1 = \left[1 + 3 \left(\frac{\sqrt{C_f}}{\kappa} \right)^2 - 2 \left(\frac{\sqrt{C_f}}{\kappa} \right)^3 \right] \quad (40)$$

649 where α_1 is a dimensionless coefficient whose value is very close to 1.0; and κ (=0.41) is von
 650 Karman's constant. Although $d\xi/dr$ is not strictly constant across the section, a representative
 651 value is sought for simplicity. A characteristic value of U is the depth-averaged velocity of a
 652 reference straight reach of the channel (U_0), characterized by a mean depth (H_0), and a roughness
 653 coefficient ($C_{f0} = C_f$). The depth-averaged s -momentum equation for the reference straight
 654 reach, assumed to have much greater width than the depth, allows U_0 to be calculated as:

$$655 \quad U_0 = \left(\frac{gH_0S_c}{c_f} \right)^{0.5} \quad (41)$$

656 Note that the product U_0 , H_0 , and B_0 (the straight-channel reference width) is Q_{bf} , which provides
 657 a check on the reasonableness of the S_c and C_f parameters selected. Using U_0 and r_c as
 658 representative values in Eq. (39) yields:

$$659 \quad \frac{d\xi}{dr} = \alpha_1 \frac{H_0S_c}{r_cC_f} \quad (42)$$

660 The current approach holds $\xi|_{r_{out}}$ constant at the outer bank floodplain elevation (η_{fp}) throughout
 661 the simulation; the remainder of the water surface is calculated according to:

$$662 \quad \xi(r) = \xi|_{r_{out}} + (r - r_{out}) \frac{d\xi}{dr} \quad (43)$$

663 At each time step, following calculation of the $\tau_{b,s}$ distribution, $\tau_{b,rt}$ is calculated using Eq. (28)
 664 and $|\tau_b|$ is calculated according to Eqs. (29) and (30).

665 4.3 Bedload Transport and Boundary Deformation

666 The magnitude of the bedload transport rate vector \mathbf{q} at each node is calculated using Eqs. (14),
 667 (15), and (17). The direction of \mathbf{q} is calculated using Eqs. (19) and (24); since Eq. (19) is an
 668 implicit equation when using the nonlinear form of A in Eq. (24), a bisection scheme is used to
 669 solve $\tan\beta$ numerically. The q_{rt} component of \mathbf{q} is calculated according to Eq. (20). Following
 670 calculation of q_{rt} at all nodes, a temporally and spatially discretized form of Eq. (7) is used to
 671 calculate the bed elevation change at each time step:

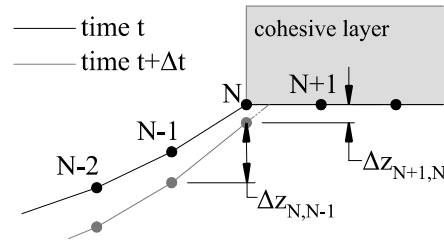
$$672 \quad \eta_i^{t+\Delta t} = \eta_i^t - \frac{1}{(1-\lambda)} \left[\frac{\Delta q_{rt}}{\Delta r} + \frac{q_{rt_i}^t}{r_i} \right] \Delta t \quad (44)$$

$$673 \quad \frac{\Delta q_{rt}}{\Delta r} = \left\{ \begin{array}{ll} \frac{q_{rt_{i+1}}^t + q_{rt_i}^t}{2\Delta r} & \text{for } i = 1 \\ \frac{q_{rt_{i+1}}^t - q_{rt_{i-1}}^t}{2\Delta r} & \text{for } i = 2 \text{ to } N - 1 \\ \frac{-(q_{rt_i}^t + q_{rt_{i-1}}^t)}{2\Delta r} & \text{for } i = N \end{array} \right\} \quad (45)$$

674 where the subscripts after variable names indicate the spatial position and the superscripts
 675 indicate the time step. The formulations for $\Delta q_{rt}/\Delta r$ at nodes 1 and N are based on the boundary
 676 conditions that $q_{rt_{1-1/2}}^t = 0$ and $q_{rt_{N+1/2}}^t = 0$, while the interior node formulation is based on
 677 central differencing.

678 4.4 Grid Translation

679 Translation of the active channel region occurs due to bedload transport processes at node N. The
 680 $q_{rt}|_{r_{out}} = 0$ boundary condition ensures that node N is degradational, provided that $\tau_b > \tau_c$ at node
 681 N; (this latter condition is described later in this section.) The slope angle that develops between
 682 node N-1 and node N is projected to the top of the noncohesive layer following boundary
 683 deformation as shown in Figure 9; the variables $\Delta z_{N,N-1}$ and $\Delta z_{N+1,N}$ are defined on the figure.
 684 When $\Delta z_{N,N-1} \leq \Delta z_{N+1,N}$, then the projected slope intersects the top of the noncohesive layer at, or
 685 to the right of, node N+1. When that occurs, then node N+1 becomes incorporated into the active
 686 channel at the next time step. All nodes $i = 1$ to N+1 are then renumbered according to: $i_{t+\Delta t} = i_t -$
 687 1. Conceptually, this assumes the upper noncohesive layer fails vertically at node N+1. The r
 688 coordinates of nodes 1 through N maintain the same values before and after the grid translation.



689

690 **Figure 9:** Bank profile that illustrates the evaluation procedure for specifying outward translation

691 Another potential cause of grid translation is mass failure within the noncohesive layer.

692 Oversteepening of the noncohesive soil to angles greater than the friction angle (Φ) will lead to
 693 shallow planar failures (Thorne, 1982). Although Φ (a mass property of the soil), and θ_{rp} (a
 694 property of grains) can potentially have different values, the two are conventionally assumed to
 695 be equivalent. This is valid in the case of an unstructured noncohesive deposit, as assumed in the
 696 present analysis; for the alternative case, see Millar and Quick, (1993) and Darby et al. (2007).

697 Oversteepening will occur when an interface develops on the slope in which $\tau_b = \tau_c$, causing the
 698 lower slope ($\tau_b > \tau_c$) to deform, while the upper slope ($\tau_b < \tau_c$) remains static. This steepens the
 699 slope near the interface and creates a topographic discontinuity (Kovacs & Parker, 1994).

700 However, the present model simulates bankfull flow, in which the noncohesive layer is always
 701 submerged. Even where the boundary shear stress becomes very small, the transverse slope
 702 steepens to the condition in which bedload transport occurs over the entire bank profile, because
 703 as ω approaches θ_{rp} , τ_c approaches zero. Extensive simulations revealed that slopes greater than
 704 θ_{rp} do not develop during the evolution toward the parallel retreat profile when using the
 705 assumption that $\Phi = \theta_{rp}$; only a specified over-step initial condition yields a situation in which a
 706 mass failure algorithm is warranted for the noncohesive bank material. Therefore, a planar
 707 failure algorithm is not relevant to the present analysis, although details of the one developed
 708 when considering sub-bankfull flow can be found in Waterman (2017).

709 4.5 Ensemble Comparison for Steady State Determination

710 In the Eulerian model framework, η changes at every node at every time step; steady state must
 711 be evaluated in this context. The number of time steps between consecutive channel shifts
 712 defines an ensemble of n_{ens} cross-sections. Once the parallel retreat condition is achieved, n_{ens}
 713 reaches a constant value or oscillates around a constant value when the time between shifts is not

714 an integer multiple of Δt . Comparisons of the η values are made with respect to two ensembles
 715 that are separated by a lateral migration distance equal to H_0 . These are referred to as Ensemble 1
 716 and Ensemble 2. The cross-sections at five discrete time positions within Ensemble 1 and
 717 Ensemble 2 are compared: $0.2n_{ens}$, $0.4n_{ens}$, $0.6n_{ens}$, $0.8n_{ens}$, and $1.0n_{ens}$. At each of these five
 718 times, the η values for that cross-section within Ensemble 1 and Ensemble 2 are compared at all
 719 spatial nodes 1 through N , and two error values, E_1 and E_2 are calculated as:

$$720 \quad E_1 = \frac{1}{5N} \sqrt{\sum_{j=1}^5 \sum_{i=1}^N (\eta_{i,Ens1} - \eta_{i,Ens2})^2} \quad (47)$$

$$721 \quad E_2 = \max_{j=1 \rightarrow 5, i=1 \rightarrow N} |\eta_{i,Ens1} - \eta_{i,Ens2}| \quad (48)$$

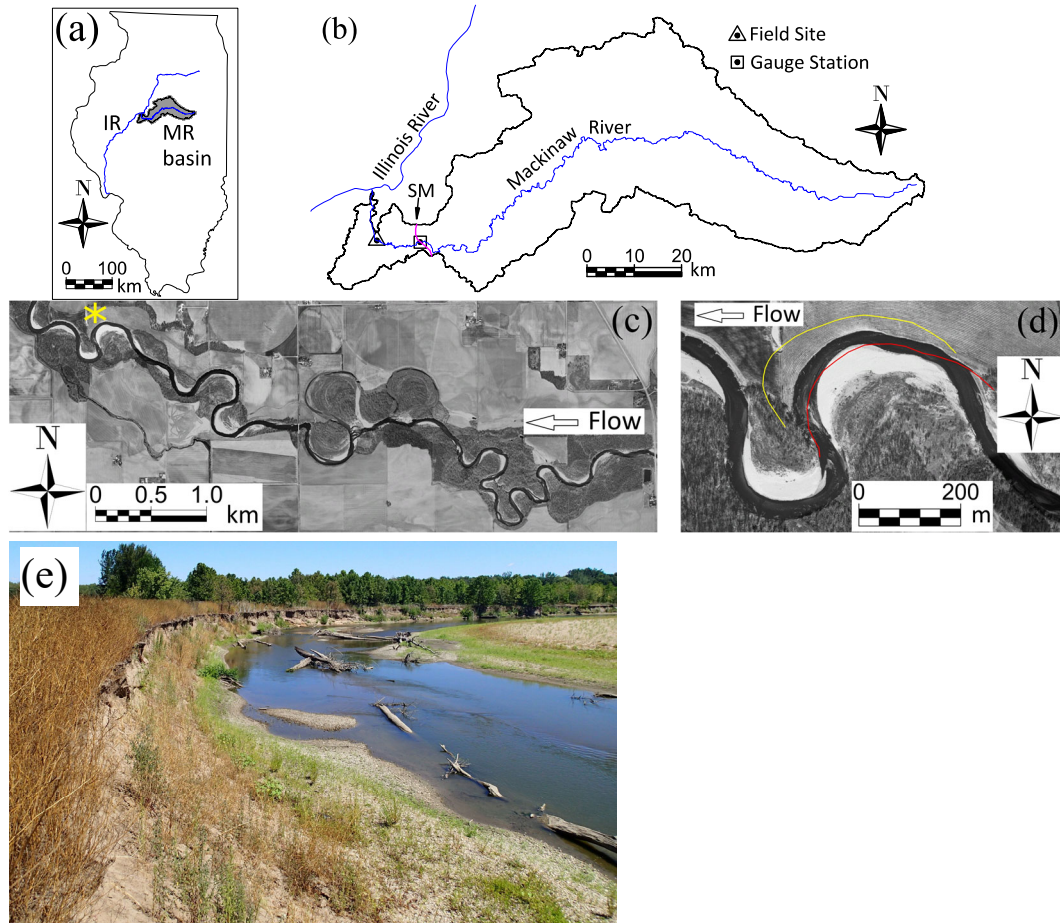
722 where the subscripts indicate the following: i , the spatial node; j , the cross-section evaluated
 723 within the ensemble; $Ens1$, Ensemble 1; and $Ens2$, Ensemble 2. The error term E_1 is the root
 724 mean square deviation over all nodes and cross-sections evaluated, and E_2 is the maximum
 725 individual deviation at a node. The steady-state criteria used requires both of the following
 726 conditions be satisfied: (a) $E_1 \leq 1 \times 10^{-5} H_0$; and (b) $E_2 \leq 1 \times 10^{-4} H_0$. Following achievement of
 727 steady-state migration, the calculated Q from Eq. (38) is evaluated according to the criteria: $|Q -$
 728 $Q_{bf}| \leq 0.001 Q_{bf}$. If the criterion is not satisfied, then the procedure begins again with an increased
 729 B value when $Q < Q_{bf}$ or a decreased B value when $Q > Q_{bf}$.

730 **5 Application of Numerical Model: Lower Mackinaw River**

731 **5.1 Study Site Description**

732 The Mackinaw River is a gravel-bed, single-thread, meandering river that is a large tributary of
 733 the Illinois River in the state of Illinois, central United States. The basin area is 2976 km^2 (Fig.
 734 10a and 10b). The river is approximately 203 km long, with a mean longitudinal slope of
 735 0.00056 and minimal slope variation along its length. The field study site and the nearest flow
 736 gauge station are located 12.7 km and 27.3 km upstream of the Illinois River confluence,
 737 respectively. The USGS (U.S. Geological Survey) gauge station, number 05568000, has been
 738 operated continuously from 1921 to 2020. The mean daily discharge is $21.9 \text{ m}^3/\text{s}$ and the 2-year
 739 recurrence interval annual series peak flow is $237 \text{ m}^3/\text{s}$; an inflection in the gauge station rating
 740 curve is present at approximately $Q = 241 \text{ m}^3/\text{s}$, which suggests overbank flow is initiated at the

741 gauge station at approximately the 2-year recurrence flow. The bankfull flow (Q_{bf}) is estimated
 742 to be 240 m³/s at the field site.



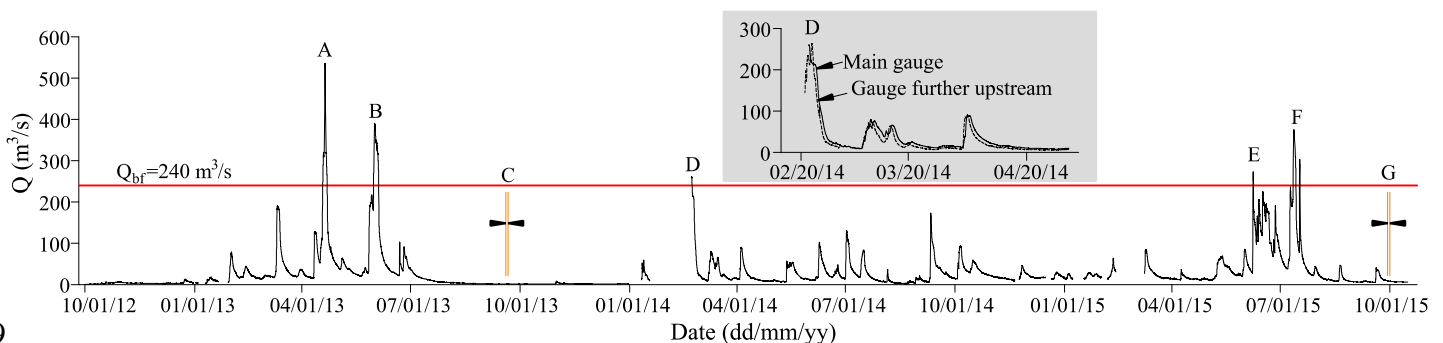
743 **Figure 10:** Illustration of the study site at increasing scales; (a) the Mackinaw River (MR) basin relative to the
 744 Illinois state boundary and the Illinois River (IR); (b) basin scale view showing location of the west terminus of the
 745 Shelbyville moraine (SM), the field site, and the stream gauge station; (c) Google Earth aerial photograph from
 746 04/02/05 of lower Mackinaw River with the study bend demarcated with the asterisk; (d) the same 04/02/05 aerial
 747 photograph zoomed into the study bend, where the red line is the digitized outer bank from 04/16/1998 and the
 748 yellow line is the digitized outer bank from 06/16/2016; (e) site photograph from 2012 looking upstream along the
 749 outer bank from the downstream end of the study bend.

750 The basin topography is dominated by a sequence of roughly parallel morainal ridges aligned in
 751 a general northwest to southeast direction, with the westernmost being the Shelbyville moraine
 752 (Fig. 10b). The Mackinaw basin west of the Shelbyville moraine is a broad valley containing
 753 predominantly sand and gravel glacial-fluvial deposits, formed by glacial outwash torrents
 754 (Johnston, 2003); these deposits have been reworked by the modern river and include post-
 755 glacial alluvium. The submorainal Mackinaw River located west of the Shelbyville moraine
 756 terminus is a geomorphically distinct unit of the river (Gough, 1994) subject to high migration

757 rates, frequent cutoffs, and a relatively large width-depth ratio, due largely to the predominantly
 758 noncohesive lower bank materials. The field site is an actively migrating bend that contains
 759 composite banks with a 4 m typical height from thalweg to top of bank. The upper cohesive layer
 760 comprises approximately half of the bank height and stands nearly vertical; the lower
 761 noncohesive layer of sand and gravel comprises the remaining half of the height and is generally
 762 convex-upward in cross-section with a much milder transverse slope. As shown in Figure 10d,
 763 the study bend has migrated extensively between 1998 and 2016; the maximum bank migration
 764 at the bend apex is 102 m, or approximately 5.6 m/yr. The lower bank commonly contains slump
 765 blocks from the upper layer that develop annual vegetation if allowed to persist for sufficient
 766 duration without being eroded (Fig 10e).

767 5.2 Field study

768 The analytical and numerical treatments represent a canonical case based on assumptions that
 769 will never be realized under real conditions. Thus, the field study was performed only to
 770 ascertain whether the canonical case reasonably approximates field conditions with respect to
 771 cross-sectional shapes and migration rates predicted. Two topographic surveys were performed
 772 using conventional total station survey methods and a local horizontal/vertical datum. The first
 773 survey was performed on September 19-20, 2013 during low flow (1.41 to 1.78 m³/s). The
 774 second topographic survey was performed on September 29-30, 2015 during moderately low
 775 flow (8.16 to 9.10 m³/s). Both surveys were performed after spring flood events with $Q > Q_{bf}$
 776 with no geomorphologically active events between the flood events and the respective surveys,
 777 with the intent for the surveys to represent reshaped channel geometry due to recent large flood
 778 events. The flow record at the gage station is illustrated in Figure 11.

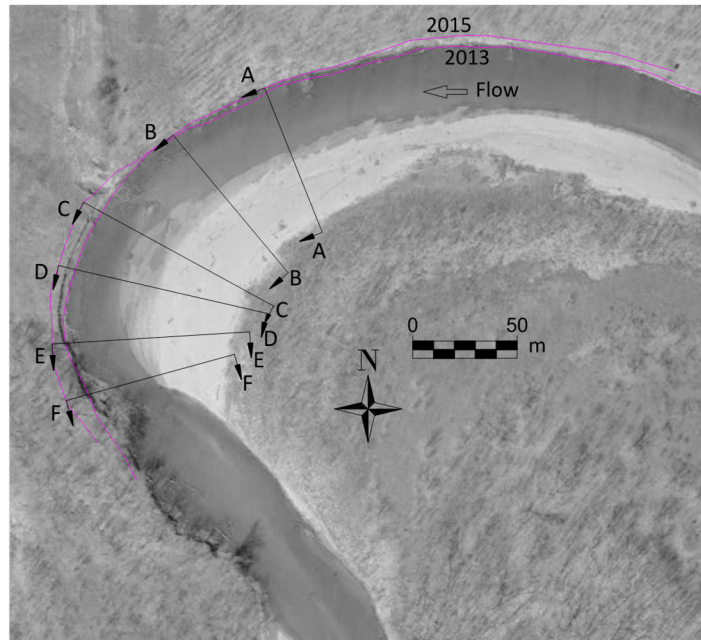


779

780 **Figure 11:** Discharge record from USGS station 05568000 just upstream of the site. The field surveys were
 781 performed during the periods labeled 'C' and 'G'. Flood events are labeled 'A', 'B', 'D', 'E', and 'F'. Periods with

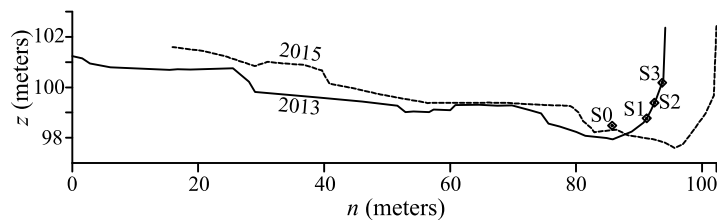
782 no data are due to ice. The gray inset that contains the event labeled 'D' includes the record from station 05568000
783 and the next gauge station upstream, 05567500; the latter captured more of the short winter event and is considered
784 to be the best available approximation of discharge conditions at station 05568000.

785 The topography was not obtained along monumented cross-sections; rather, data points were
786 collected to represent full coverage of the banks, channel, and point bar. The 2015 topographic
787 survey focused on the downstream portion of the bend subjected to the highest migration rates. A
788 triangular-irregular-network (TIN) was created for each survey, and the topography for the cross-
789 sections were sampled from the TINs. The cross-sectional locations are shown in Figure 12.
790 Each cross-section had similar characteristics when comparing the 2013 and 2015 data, with the
791 sections translated outward with discernible but minor changes in shape. In Figure 13, Cross
792 Section D illustrates representative conditions; at this section, the data transects on the banks
793 from 2013 and 2015 were directly in alignment, and thus, interpolation errors associated with
794 sampling from the TIN in the bank region are minimized. Between cross sections C and F, the
795 channel migrated an average of 8.15 m with a maximum of 10.8 m; the average was obtained by
796 calculating the area between the top of bank lines shown on Figure 12 and dividing by the
797 average length of the top of bank lines between those sections. In addition to the topographic
798 data, surface soil samples of the bank were collected and surveyed in 2013 between Cross
799 Sections C and D. The locations of these samples are shown on Figure 13. From the water line to
800 the top of the noncohesive layer, the soil became finer-grained upwards in a similar manner to
801 that observed on the point bar. The grain-size distributions are illustrated in Figure 14.



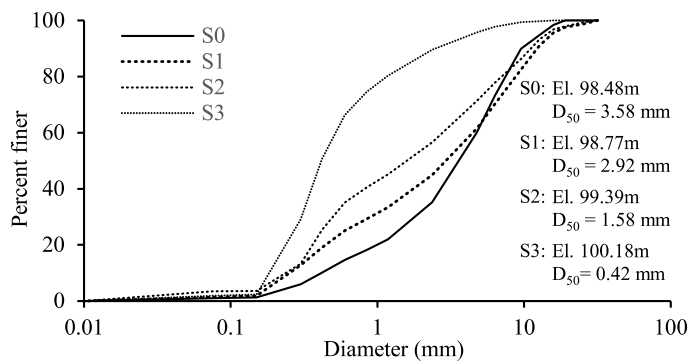
802

803 **Figure 12:** Cross sections from topographic survey overlain on the Google Earth aerial photograph from
 804 04/17/2014. The two magenta lines are the surveyed top of bank from the field surveys in 2013 and 2015.



805

806 **Figure 13:** Cross-section D as surveyed in 2013 and 2015. The transverse coordinate n is used, where $n = 0$ is
 807 relative to the end of the cross-section illustrated in Figure 12. The vertical is exaggerated 4x. The marks S0 through
 808 S3 are the locations of the surface soil samples. Sample S0 was from a low midchannel bar located off the cross-
 809 section; S1, S2, and S3 were sampled on the bank.



810

811 **Figure 14:** The grain-size distributions of the bank and bar samples.

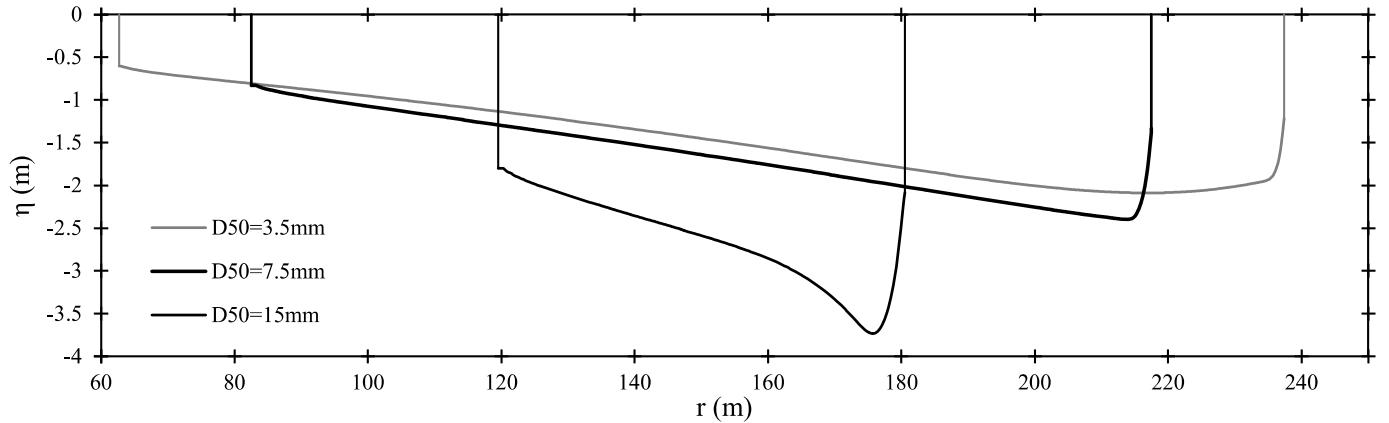
812

813 5.3 Numerical model results and comparison with field data

814 The results of three different simulations are illustrated; all parameters used in the simulations
 815 are identical, except the D_{50} and τ_{c0}^* values. Simulation 1 has $D_{50} = 3.5$ mm and $\tau_{c0}^* = 0.036$.
 816 Simulation 2 has $D_{50} = 7.5$ mm and $\tau_{c0}^* = 0.040$. Simulation 3 has $D_{50} = 15.0$ mm and $\tau_{c0}^* =$
 817 0.045 . As few grains were recorded in the sediment samples with $D > 15$ mm (maximum 4%
 818 mass for grains coarser than 15 mm in sample S1), simulations were not extended to greater D_{50}
 819 values. The full list of parameters is provided in Table 1. The values for B_0 and r_c were estimated
 820 based on aerial photograph analysis; H_0 was an estimate based on field observations; S_c was
 821 based on longitudinal profiles of the river (Gough, 1994); and Q_{bf} was based on data analysis
 822 from the nearby gage station. Figure 15 and Table 2 illustrate the results of the simulations.

823 **Table 1:** List of parameters used in the numerical simulations. The equation column indicates how the parameter is
 824 used in the numerical model; the parameter may be in other equations that are part of the analytical treatment that
 825 are not provided in the table.

Parameter	Value	Eqn.
B_0 (m)	50.0	41
C_f	0.0059	37, 40
D_{50} (mm)	3.5	18, 20
H_0 (m)	3.0	41
K_0	5.7	17
K_l	10	28
Q_{bf} (m ³ /s)	240	38
r_c (m)	150	34, 35
R_s	1.65	18, 20
S_c	0.00056	34, 35
Δr (m)	0.1	36, 45
Δt (s)	30	44
θ_{rp} (°)	40	15, 16, 24
λ	0.40	44
μ_d	0.5	24
τ_{c0}^*	0.036	14, 17, 18, 19
χ	1.0	24



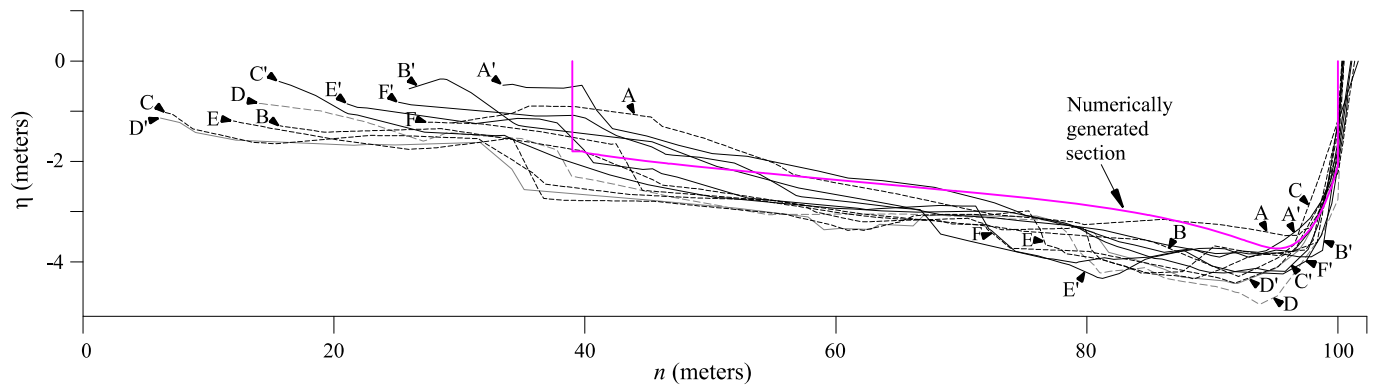
827
828 **Figure 15:** The steady-state migrating cross-sections for the three simulation conditions. Vertical lines are used to
829 illustrate the lateral boundaries (cohesive top layer on right bank; vegetated over-bar region on left bank).

830 **Table 2:** Results of numerical simulations.

	Sim. 1 $D_{50}=3.5$ mm $\tau_{c0}^*=0.036$	Sim. 2 $D_{50}=7.5$ mm $\tau_{c0}^*=0.040$	Sim. 3 $D_{50}=15.0$ mm $\tau_{c0}^*=0.045$
B (m)	174.7	135.0	61.0
r_{thal} (m)	216.80	213.85	175.65
$\eta _{r_{out}}$ (m)	-1.221	-1.335	-2.085
$\eta _{r_{thal}}$ (m)	-2.088	-2.400	-3.735
$h _{r_{thal}}$ (m)	2.05	2.39	3.73
$\tau_{s _{r_{thal}}}^*$	0.137	0.0735	0.0611
c_0	0.999	0.969	0.848
$q_{rt} _{r_{thal}}$ (m^2/s)	-1.45×10^{-5}	-1.05×10^{-5}	-1.96×10^{-5}
$\int_{r_{thal}}^{r_{out}} \frac{q_{rt}}{r} dr$ (m^2/s)	-1.14×10^{-6}	-1.32×10^{-7}	-3.74×10^{-7}
M (m/day)	2.21	1.40	1.67

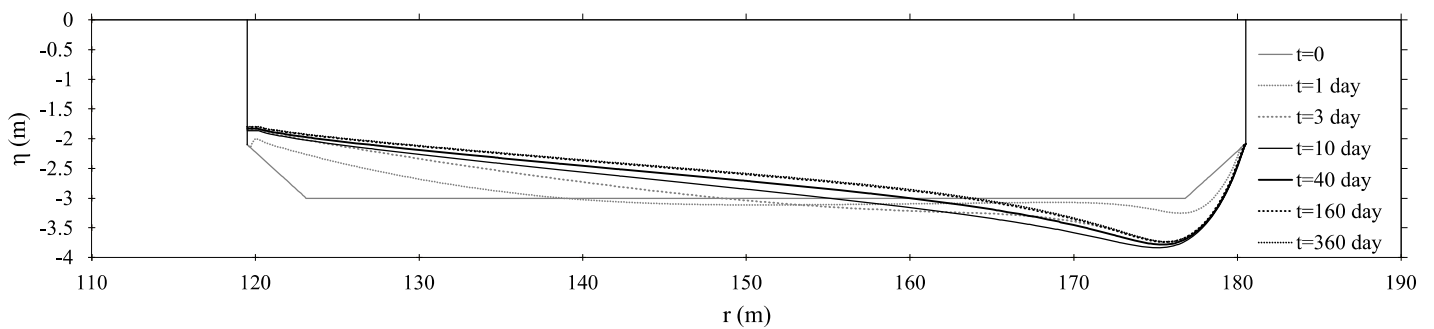
831 The η values are relative to a vertical datum at the floodplain surface elevation (top of cohesive
832 layer); c_0 is back-calculated from Eq. 26(a) using the outputs of the hydrodynamic variables. The
833 M values are the migration rates recorded in the simulations; when using the model outputs of
834 sediment transport rates and geometry variables, all migration rates were confirmed to be
835 equivalent to the calculated value using Eq. (25). Simulation 1 has the sediment parameters that
836 best represent the field data, but the result does not accurately represent the cross-sectional shape
837 observed in the field; increasing D_{50} and τ_{c0}^* for Simulations 2 and 3, the results approach the
838 observed cross-sectional shapes. The simulation results suggest the Mackinaw River behaves
839 according to a considerably higher τ_{c0} than that indicated by the grain size distribution observed

840 in the field, which is a key issue discussed in the Discussion and Conclusions. The numerically
 841 generated cross-section and field surveyed sections are compared in Figure 16.

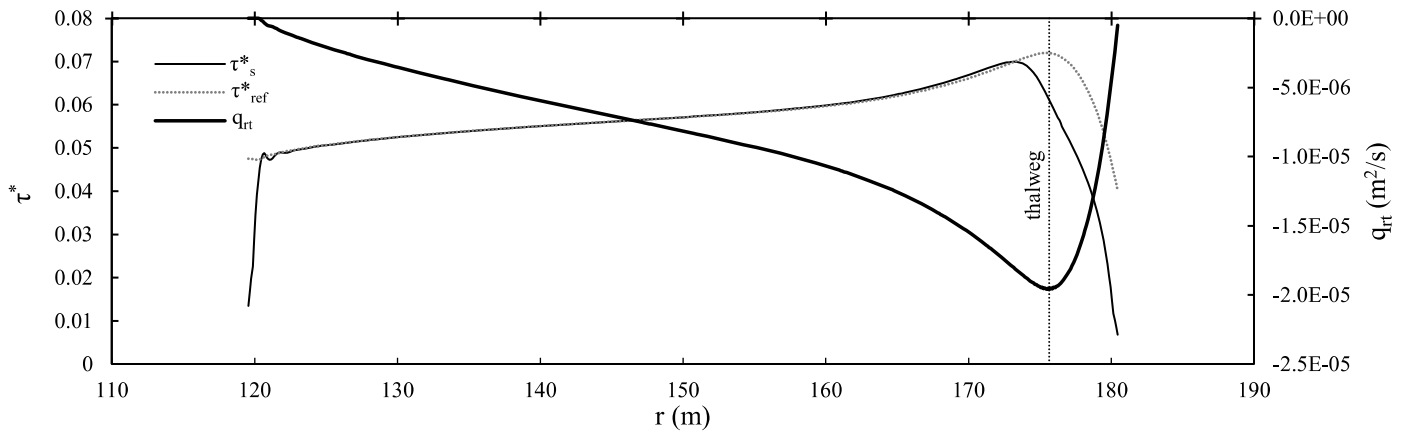


842
 843 **Figure 16:** The black cross-sections are Cross Sections A through F surveyed in 2013 (dashed lines) and 2015 (solid
 844 lines, section name appended with '). Positions of cross-sections are shown on Fig. 12. All cross-sections are placed
 845 on same frame of reference for comparison by setting top of bank elevation to $\eta = 0.0$ m; and the n position of the
 846 top of noncohesive layer to 100.0 m. The magenta line is the numerically generated cross-section using $D_{50}=15$ mm
 847 and $\tau_{c0}^*=0.045$.

848 Figure 17 illustrates a time series of the cross-section evolution from an arbitrary initial condition
 849 to the steady-state configuration for the simulation with $D_{50} = 15$ mm. As the water surface
 850 elevation is kept steady in time, the discharge changes until the steady-state configuration is
 851 achieved. Figure 18 illustrates the distribution of τ_s^* and q_{rt} associated with the steady-state
 852 configuration.



853
 854 **Figure 17:** Time evolution of the simulation performed with $D_{50} = 15$ mm and $\tau_{c0}^* = 0.045$.



855

856 **Figure 18:** Steady-state distribution of τ_s^* and q_{rt} for the simulation performed with $D_{50} = 15$ mm and $\tau_{c0}^* = 0.045$.
 857 Note that τ_{ref}^* is a calculated reference value based on $\tau_b = \rho ghS$, which neglects momentum extraction due to shear
 858 on transverse faces.

859 The numerical model simulates migration under a steady Q_{bf} . The meander bend at the field site
 860 underwent migration and cross-sectional reshaping over a range of flows that included Q_{bf} ;
 861 therefore, comparison of the migration rates between the field site and the simulations are
 862 approximate and indicate only whether the migration rates are on the right order of magnitude.
 863 Between the 2013 and 2015 surveys, the surveyed region in Fig. 12 experienced an average
 864 migration distance of 8.15 m (maximum 10.8 m). Using the 15-minute time series at the USGS
 865 gage station, $Q \geq Q_{bf}$ was experienced for 3.26 days between the surveys; and $Q \geq 0.8Q_{bf}$ was
 866 experienced for 10.54 days. Assuming migration only occurred when $Q \geq Q_{bf}$ suggests a mean
 867 migration rate of 2.5 m/day and assuming migration occurred throughout the period $Q \geq 0.8Q_{bf}$
 868 suggests a mean migration rate of 0.77 m/day. The simulation result of 1.67 m/day migration rate
 869 lies between these two values, and thus, it suggests the simulated migration rate is within the
 870 proper order of magnitude. As another check on the reasonableness of the results, the aerial
 871 photograph illustrated in Fig. 10d shows digitized bank lines over the 18.2-year period of
 872 migration between 1998 and 2016. The maximum migration rate was 102 m. Using the 15-
 873 minute time series, $Q \geq Q_{bf}$ was experienced for 47.8 days during this time period; and $Q \geq$
 874 $0.8Q_{bf}$ was experienced for 81.9 days. Assuming migration only occurred when $Q \geq Q_{bf}$ suggests
 875 a mean migration rate at the locus of maximum migration equal to 2.1 m/day and assuming
 876 migration occurred throughout the period $Q \geq 0.8Q_{bf}$ suggests a mean migration rate of 1.1
 877 m/day. As before, the results suggest the order of magnitude predicted by the simulations is
 878 correct.

879 **6 Discussion and Conclusions**

880 6.1 General Considerations

881 The analysis presented is a conceptualization intended to shed light on bank erosion and channel
882 migration when noncohesive bank material is a dominant factor. Such a treatment highlights key
883 physical processes and provides a basis for comparison with observations to provide clues to
884 those factors responsible for deviations from the canonical case. The three objectives outlined in
885 the Introduction were resolved: (a) a rational constraint on the bank shape was established ($\omega|_{r_{thal}}$
886 $=0$); (b) a migration rate formulation was developed (Eq. 32); and (c) parallel retreat was shown
887 numerically to develop as conceived in the analytical treatment as a simple outward translation
888 of the cross-section rather than involving a cyclic process of basal erosion and mass failure in the
889 noncohesive layer. The findings reveal important differences to past treatments; they also
890 highlight important aspects of channel shape and misunderstandings that can result from usage of
891 the linear excess shear stress formulation (Eq. 1) when modeling bank deformation in
892 noncohesive materials.

893 The analytical treatment focused on the development of a steady-state migration rate equation
894 based on integration of the Exner equation over the bank region following the logic of Hasegawa
895 (1989), which requires calculation of $q_{rt}|_{r_{thal}}$. Since $q_{rt}|_{r_{thal}}$ is dependent on the local transverse slope
896 at the limit of integration, the slope should not be assigned arbitrarily. The $\omega|_{r_{thal}}=0$ shape
897 constraint determined theoretically and confirmed numerically yields a substantially different
898 migration rate equation than that of Hasegawa (1989), due to a change in the dominant factors
899 that dictate $q_{rt}|_{r_{thal}}$, which drives migration. Equation (19) indicates that the decomposition of q at
900 any point has a contribution associated with secondary flow (the term containing $\tan \delta$) and a
901 contribution associated with transverse slope (the term containing $\tan \omega$). Whereas Hasegawa
902 (1989) determined that the contribution from secondary flow was small enough to be neglected,
903 the current analysis finds that the contribution from the secondary flow is responsible for the
904 entirety of the transverse component of the bedload transport rate at the thalweg when
905 considering the case of parallel retreat. This yields a migration rate equation (Eq. 32) that is
906 dependent on curvature, unlike previous forms of migration rate developed using the integral
907 treatment. Previous bank-integrated migration rate formulations implicate the helical flow

908 associated with curvature indirectly, as it is responsible for a deeper channel near the outer bank,
 909 which results in excess velocity or excess boundary shear stress near the outer bank. The present
 910 model more directly implicates the importance of curvature in the migration process as the
 911 primary driver of the transverse rate of bedload transport due to the helical flow. The migration
 912 rate formulation developed also generalizes to the case of a straight channel, in which $r = \infty$ and
 913 consequently $M = 0$.

914 The analysis supports a finding of Stecca et al. (2017), who evaluated a number of variables for
 915 suitability as independent variables in lumped noncohesive bank migration formulations. Among
 916 the variables analyzed, the downstream component of sediment transport rate at the basal node
 917 was deemed among the most promising. The current analysis indicates the physical basis of this
 918 finding, in that the migration rate is based on $q_{rt}|_{r_{thal}}$ which is directly related to $q_s|_{r_{thal}}$ through the
 919 variable β (which is equal to δ at the thalweg). Another interesting finding is that the Selwyn
 920 River cross-sections they analyzed for a hydrograph that produced bankfull flow resulted in
 921 cross-sections that maintained their general shape after undergoing a migration distance of > 15
 922 m, similar to that documented in the present study. The shapes were also qualitatively similar to
 923 those of the present study, being concave-upward on the bank and across the thalweg and
 924 transitioning to convex-upward on the bar.

925 A substantial body of research has addressed equilibrium channel cross-sectional geometry in
 926 straight channels with noncohesive banks and equilibrium point bar geometry when the outer
 927 bank is fixed (nonmigrating). A migrating channel differs from both scenarios. The past
 928 treatments involved the channel achieving a shape such that $q_{rt} = 0$ everywhere on the section.
 929 The current treatment does not invalidate those approaches; however, it does show that such a
 930 solution is specific to the case in which $M = 0$. The more general solution is expressed in Eq.
 931 (10), which is valid for either a migrating or non-migrating steady-state condition. For $M > 0$, q_{rt}
 932 will be negative across the section except near the boundaries (where $q_{rt} = 0$ as specified
 933 boundary conditions). This is illustrated in the numerical results of Fig. 18 but can also be
 934 substantiated theoretically. At the thalweg, a negative q_{rt} is ensured due to the secondary flow
 935 direction in conjunction with the $\omega|_{r_{thal}} = 0$ shape constraint. Assuming that the value q_{rt}/r is small,
 936 Eq. (10) indicates the negative q_{rt} will be approximately the local minimum ($\partial q_{rt}/\partial r \approx 0$ where
 937 $\partial \eta/\partial r = 0$). Moving in the positive r direction (bankward of the thalweg), where $\partial \eta/\partial r$ is positive,

938 Eq. (10) requires a less negative q_{rt} that will transition to $q_{rt} = 0$ at the boundary. Moving in the
939 negative r direction, where $\partial\eta/\partial r$ is negative, Eq. (10) also requires a less negative q_{rt} that will
940 transition to $q_{rt} = 0$ at the boundary. The analysis has not advanced to the point of being able to
941 specify $\eta|_{r_{thal}}$ or r_{thal} without the use of the numerical model. However, if these variables could be
942 predicted, it is conceivable that Eq. (10) could be used to calculate steady-state migrating shapes
943 analytically in an analogous manner to past work using the $q_{rt} = 0$ solution criteria (e.g., Kikkawa
944 et al., 1976). Such an analysis would be most practicable interior to the thalweg (well away from
945 the outer bank), where the boundary shear stress is readily determined as a function of the local
946 flow depth (see Fig. 18).

947 While the exact cross-section shape still cannot be specified without detailed numerical analysis
948 of the hydrodynamics and the transverse boundary layer associated with the outer bank, both the
949 analytical and numerical treatments indicate that the shape will have differences relative to the
950 characteristic cross-section of Parker et al. (2011) depicted in Fig. 6. The convex-upward shape
951 of the region left of the thalweg in Fig. 6 is based on the $q_{rt} = 0$ solution criterion used for
952 predicting the transverse slope on the point bar. The convex-upward shape on the bar is valid,
953 although the results illustrated here suggest that the convexity is poorly pronounced during
954 steady-state migration, having only a slight camber similar to the point bar platforms described
955 by Nanson (1980), on top of which scrolls of finer-grained suspended material were deposited.
956 Further comparison with the characteristic cross-section of Parker et al. (2011) reveals more
957 significant differences at the thalweg and in the bank region. A concave-upwards shape develops
958 interior to the thalweg, with a horizontal transverse slope at the thalweg, and with the concave-
959 upward shape continuing throughout the noncohesive layer bankward of the thalweg. This is
960 contrasted with the grade break at the thalweg in Parker et al. (2011) in which the convex-
961 upward topography interior to the thalweg abruptly changes to a uniform slope in the bank
962 region. The Mackinaw River field data provides one example that the cross-sectional shape
963 suggested by the present analysis is more realistic for a migrating meander bend with composite
964 banks.

965 The concave upward shape within the noncohesive material in the bank region directly
966 contradicts the shape suggested by use of the linear excess shear stress equation (Eq. 1) to model
967 noncohesive fluvial erosion. Applying Eq. (1) to bank materials consisting of uniform soil

968 properties suggests the following: (a) because the boundary shear stress generally increases with
969 depth, the erosion rate will be greatest near the base of the bank, thus, leading to steepening in
970 the presence of excess boundary shear stress; (b) continued steepening leads to an unstable bank
971 slope that exceeds the soil friction angle and large-scale mass failure involving much of the bank
972 height; (c) after failure, the basal material must be removed by fluvial action; and (d) the cycle
973 repeats. Such cyclical behavior would violate the basic assumptions of the parallel retreat
974 conceptualization of a bank migrating without changing shape. While the cyclical sequence
975 described accurately characterizes the process for cohesive bank erosion, it inaccurately
976 characterizes the process for noncohesive bank materials mobilized as bedload. When
977 implementing the Exner equation with a suitable bedload transport relationship, a boundary shear
978 stress distribution that increases with depth does not cause a bank slope to steepen with depth,
979 but rather causes the slope to relax with depth. The development of a concave-upward
980 noncohesive bank shape in the presence of excess boundary shear stress has been well
981 documented experimentally in straight channels (e.g., Ikeda et al., 1981). As is borne out by the
982 present analysis, the resulting shape does not fundamentally change simply due to the addition of
983 planform curvature. The primary difference between the straight channel case and the bend flow
984 case is that the helical flow serves to drive a transverse component of bedload away from the
985 base of the outer bank. This allows the bank to migrate when subjected to excess shear stress
986 rather than aggrading the base and relaxing its slope to a threshold channel configuration as
987 occurs in the absence of the helical flow. One way to generalize between straight and curved
988 channels is by conceiving of a “demand” for bed material imposed by the removal of sediment at
989 the base of the bank in the transverse direction, following Thorne (1982) regarding unimpeded
990 removal of basal material. When the channel is straight, the bed material demanded at the base of
991 the bank is zero; when the channel has curvature, the demand is non-zero. This demand is
992 satisfied through the adjustment of bank shape, which affects both the boundary shear stress
993 distribution and the transverse component of bedload. Thus, analogous to the concept of a graded
994 channel which delicately adjusts its longitudinal slope to convey exactly the sediment fed into
995 the stream with the available discharge (e.g., Mackin, 1948), the steady-state migrating channel
996 delicately adjusts its transverse slope to satisfy the demand for material at the base of the bank in
997 a manner that conforms with Eq. (10).

998 The findings also shed light on laboratory experiments involving meandering channels in
999 noncohesive materials. With reference to Fig. 3, two primary reasons can be identified for the
1000 difficulty in achieving a condition approximating parallel retreat in laboratory experiments of
1001 meander bend evolution: (a) vegetation establishment and consequent fine sediment deposition
1002 in over-bar Region 3 is not able to suitably constrain the channel geometry on the inner bend;
1003 and (b) $\eta|_{r_{out}}$ is commonly set too high on the outer bank relative to the elevation at which the
1004 sediment can be transported at the inside of the bend, which creates the condition in which the
1005 cross section will be net aggradational as it migrates, as demonstrated in Appendix A. This
1006 widening and shallowing of the channel during migration ultimately devolves into a braided
1007 channel form. Both conditions could potentially be mitigated through appropriate experimental
1008 setup and procedures undertaken during an experiment to artificially incorporate point bar
1009 vegetation. However, a third issue of bank stiffening to artificially slow the outer bank migration
1010 appears to be an additional step that is warranted to best represent prototype conditions based on
1011 the present findings. As evidence, the Mackinaw River appears to behave as if the critical shear
1012 stress is considerably larger than that indicated by its grain-size distribution. This is discussed
1013 further in the following subsection.

1014 6.2 Limitations and Practical Considerations

1015 The highly conceptualized scenario analyzed in this study is a gross simplification of the
1016 complexities of real rivers; it is intended as a canonical case. Nevertheless, some practical
1017 application of the analysis can be anticipated for use in lumped bank erosion models. The
1018 concepts developed would be most useful in a lumped bank erosion model if a similarity
1019 function for the bank shape had been obtained. The analysis did not progress to the stage of
1020 being able to specify such a function. Nevertheless, the demonstration of the concave-upward
1021 bank shape with the $\omega|_{r_{thal}}=0$ shape constraint that precludes a cyclical process of oversteepening
1022 and mass failure in coarse noncohesive bank materials has significant modeling implications.
1023 The $\omega|_{r_{thal}}=0$ shape constraint that is valid for steady-state migration seems to reasonably
1024 represent the field data, and this constraint allows ready calculation of the transverse component
1025 of the bedload transport rate that drives the bank migration rate in either Eq. (25) or Eq. (32).
1026 Figure 18 shows that the bank maintains its concave upward shape during shape evolution, and
1027 thus, the $\omega|_{r_{thal}}=0$ shape constraint appears reasonable even during unsteady-state migration. The

1028 numerical model whose bank erosion treatment most closely approximates the present treatment
1029 is that of Nays2DH (Shimizu et al., 2014; Eq. 129 therein). In that model, a bank erosion
1030 formulation nearly equivalent to Eq. (25) is used, although it incorporates an additional term
1031 based on aggradation or degradation of the basal node. The basal node elevation change is from
1032 an independent Exner equation calculation that incorporates the spatial derivatives of the
1033 sediment transport vector \mathbf{q} in both the r and s directions. That model or any other model that
1034 explicitly calculates \mathbf{q} at the basal node can readily incorporate the $\omega|_{r_{thal}}=0$ shape constraint to
1035 better approximate a similarity function over the bank region rather than assuming the basal node
1036 represents an abrupt grade break associated with a bank of constant slope.

1037 Any model that simulates hydrographs of individual events must recognize that a variable
1038 discharge will result in bank reshaping not accounted for in a lumped bank erosion model that
1039 assumes a similarity function for bank shape. A change in the bank shape will yield periods
1040 where the top of bank migrates greater and lesser distances than that suggested by the transverse
1041 flux of sediment at the base. However, over long periods of time, such as dealt with in models
1042 such as RVR Meander (Abad & García, 2006; Motta et al., 2012), these transient periods of bank
1043 reshaping will average out, and the volume of sediment transported transversely across the
1044 thalweg will approach the volume of noncohesive bank material contained in the calculated
1045 migration distance. Models such as RVR Meander that assume a cross-sectional form rather than
1046 calculating bed evolution explicitly using the Exner equation present additional complications
1047 with respect to specifying r_{thal} , $\eta|_{r_{thal}}$, and c_0 when using the migration rate equation. With the
1048 present state of knowledge, these terms cannot be predicted *a priori*; a user would need to
1049 develop relationships for these variables as a function of centerline radius (or δ) using either a
1050 detailed numerical model such as that in Section 4 or obtaining field data to develop reasonable
1051 relationships. The complication is that the numerical model of Section 4 is mechanistic and
1052 requires no arbitrary parameters but is not free of requiring calibration. The Mackinaw River
1053 application showed that applying the field grain size distribution yields unrealistic results in
1054 terms of the cross-sectional shape. Effectively, a calibration process was required in Section 5 in
1055 which D_{50} was increased to make the numerical results reasonably represent the field data. This
1056 suggests the mechanistic numerical model is lacking important processes or is poorly
1057 characterizing those processes it simulates. Sufficient analyses have not been performed to
1058 indicate whether the good calibration result obtained was simply fortunate or is more generally

1059 applicable. Regardless, the model obviously and intentionally neglects important physical
1060 factors, with implications for applying the results. Almost innumerable factors could be cited that
1061 were neglected which may be important in certain circumstances, but several major factors stand
1062 out as warranting elaboration: (a) the hydrodynamic treatment; (b) sediment sorting and
1063 stratification; (c) and the mechanics of the cohesive top layer.

1064 First, the hydrodynamic treatment assumed a hydrostatic pressure distribution in the vertical,
1065 which neglects the effects of vertical accelerations that are likely important close to the bank.
1066 Transverse and vertical transport of downstream momentum were neglected, and the radial
1067 component of momentum was not explicitly solved. Such simplifications were necessary to
1068 obtain boundary shear stress distributions quickly due to the large number of time steps required
1069 to achieve the steady-state migration. Applying a more sophisticated three-dimensional
1070 nonhydrostatic hydrodynamic model with the boundary shape obtained by the simplified model
1071 would be worthwhile to ascertain whether the τ_b distribution (both magnitude and direction) in
1072 the near-bank region is realistic or warrants substantial improvement. A further hydrodynamic
1073 issue is that form drag was not accounted; if form drag was significant, the τ_b associated with
1074 skin friction that drives sediment motion would be reduced. Decreasing τ_b to account for form
1075 drag has the same effect on migration rate as artificially increasing τ_{c0} as was done in Section 5,
1076 decreasing the excess shear stress term. Secondly, given the fining upward grain size distribution
1077 observed in both the banks and the point bar at the field site, the issue of sorting and stratigraphy
1078 (e.g., Parker & Andrews, 1985) is clearly significant in determining the shape of both bar and
1079 banks. The present model assumes a single grain size; it takes no account of different τ_{c0} and
1080 transport deviation angles of sediment grains based on grain size. The concentration of large
1081 diameter grains at the base of the bank common in bends may limit the transverse component of
1082 bed material transport across the thalweg, thus slowing the migration rate due to the reduced
1083 demand for bank material. Focusing strictly on the bank, in addition to the modified τ_{c0} and
1084 transport deviation angles associated with grain size, the structure of the bank material is also not
1085 incorporated into the model. The banks at the field site were not comprised of loose, unstructured
1086 deposits as assumed in the model; they were structured deposits with interlocked grains that
1087 certainly influences τ_{c0} and θ_{rp} (Millar & Quick, 1993). Third, the effect of the cohesive top layer
1088 on bank migration processes is significant when it comprises a large percentage of the bank
1089 height, as in the Mackinaw River. Mass failure of the material yields slump blocks that influence

1090 τ_{c0} of the lower bank and mitigates migration rates (e.g., Parker et al., 2011). The current analysis
1091 has made no attempt to decipher the relative effects of these and other complicating factors, but
1092 for the Mackinaw River case, the analysis strongly suggests that additional factors are playing a
1093 significant role in determining cross-sectional shape and migration rate than that included in the
1094 simplified model. Whether the sum of these unaccounted effects can be reasonably represented
1095 for application on most rivers by increasing D_{50} (and consequently τ_{c0}) as in the Mackinaw River
1096 case requires further exploration.

1097 Finally, application of the modeling approach developed in Section 4 outside the framework of a
1098 lumped bank erosion model in a high-resolution cross-section-based model such as BSTEM or
1099 CONCEPTS is beyond the scope of the present analysis. However, a few obvious considerations
1100 warrant highlighting. A morphologically active flow below the top of the noncohesive layer will
1101 generate an interface on the bank that separates a lower region subject to fluvial erosion, and an
1102 inactive upper region. In such an event, oversteepening and shallow planar mass failures would
1103 be expected within the noncohesive layer, and such a process would need to be incorporated into
1104 such a model. The mechanics of the upper cohesive layer, including both fluvial erosion and
1105 mass failure, would also need to be explicitly incorporated.

1106 **Acknowledgments**

1107 This work was funded by the Illinois Water Resources Center (Grant: Streambank Erosion in the
1108 Mackinaw River, Illinois) when the first author was a graduate student at University of Illinois at
1109 Urbana-Champaign. Thanks are extended to the following: Gary Parker and Davide Motta for
1110 many helpful discussions during the analysis; Zhenduo Zhu and Dimitrios Fytanidis for
1111 assistance with field work; Don Rollo, the property owner, for cooperation with field work and
1112 allowing access to the site.

1113 **Appendix A**

1114 The volume of bed material sized sediment eroded per unit length of centerline in the region $r >$
1115 r_{thal} is defined as \mathcal{V}_e ; the volume deposited in the region $r \leq r_{thal}$ is defined as \mathcal{V}_d . For steady-state
1116 migration to be possible, \mathcal{V}_e must equal \mathcal{V}_d within each unit of time. The volumetric erosion and
1117 deposition rates are expressed in Eqs. (A1) and (A2), respectively; each equation contains an

1118 exact and an approximate form, in which the latter are the solutions of the integrals based on an
 1119 assumed linear relationship between η and r .

$$1120 \quad \frac{\partial \Psi_e}{\partial t} = \int_{\eta|_{r_{thal}}^{\eta|_{r_{out}}} (1 - \lambda) M \frac{r}{r_c} dz \approx M(\eta|_{r_{out}} - \eta|_{r_{thal}})(1 - \lambda) \frac{(r_{out} + r_{thal})/2}{r_c} \quad (A1)$$

$$1121 \quad \frac{\partial \Psi_d}{\partial t} = \int_{\eta|_{r_{thal}}^{\eta|_{r_{in}}} (1 - \lambda) M \frac{r}{r_c} dz \approx M(\eta|_{r_{in}} - \eta|_{r_{thal}})(1 - \lambda) \frac{(r_{thal} + r_{in})/2}{r_c} \quad (A2)$$

1122 The equivalence between Eqs. (A1) and (A2) in their exact form is expressed in Eq. (A3):

$$1123 \quad \left(\int_{\eta|_{r_{thal}}^{\eta|_{r_{out}}} r dz \right) \Big|_{r > r_{thal}} = \left(\int_{\eta|_{r_{thal}}^{\eta|_{r_{in}}} r dz \right) \Big|_{r \leq r_{thal}} \quad (A3)$$

1124 Eq. (A3) is based on the problem definition that M and r_c are constant, along with an assumption
 1125 of constant λ . The functional relationship between η and r is not known *a priori*; but regardless
 1126 of this relationship, the r values are uniformly larger in the left-hand-side than the right-hand-
 1127 side of Eq. (A3). This requires that $\eta|_{r_{out}}$ must be less than $\eta|_{r_{in}}$ to achieve the equivalence since the
 1128 lower limits of the integral are equal. This is demonstrated more intuitively using the
 1129 approximate form of Eqs. (A1) and (A2). Equating the erosion rates and deposition rates yields:

$$1130 \quad \frac{(r_{thal} + r_{in})}{(r_{thal} + r_{out})} \approx \frac{(\eta|_{r_{out}} - \eta|_{r_{thal}})}{(\eta|_{r_{in}} - \eta|_{r_{thal}})} \quad (A4)$$

1131 In Eq. (A4), the left-hand-side is necessarily less than unity, which consequently requires that
 1132 $\eta|_{r_{out}}$ be less than $\eta|_{r_{in}}$. For the numerical analysis of Section 5, the most physically reasonable
 1133 value of $\eta|_{r_{out}}$ is the maximum value of $\eta|_{r_{in}}$ at which sediment can be transported and deposited,
 1134 assuming that the outer bank is a previously formed inner bend lateral accretion deposit.
 1135 However, Eqs. (A3) and (A4) indicate a steady-state solution does not exist for $\eta|_{r_{out}} = \eta|_{r_{in}}$. If $\eta|_{r_{out}}$
 1136 is established too high on the bank, then more volume is eroded outside the thalweg than can be
 1137 deposited inside the thalweg as the steady-state geometry is approached. The result is that the
 1138 channel continually aggrades until no portion of the channel cross section is competent to
 1139 transport sediment ($M = 0$), which is not a viable equilibrium geometry if the stream has any bed
 1140 material sediment load. These considerations constrain the elevation of $\eta|_{r_{out}}$ since it must be less

1141 than $\eta|_{r_{in}}$, while $\eta|_{r_{in}}$ has a physical limit based on the maximum elevation at which bankfull flow
 1142 is competent to transport sediment.

1143 The approach used herein to calculate $\eta|_{r_{out}}$ is an approximation based on Eq. (A4) that is
 1144 primarily intended to establish $\eta|_{r_{out}}$ consistently over a range of conditions rather than suggesting
 1145 a rigorous value of $\eta|_{r_{out}}$ based on physical principles. The variables r_{thal} , $\eta|_{r_{thal}}$, and $\eta|_{r_{in}}$ in Eq. (A4)
 1146 are not known *a priori*; in fact, the first two are key variables being sought in the numerical
 1147 solution. The first of these terms is approximated as $r_{thal} = r_{out}$, and the left-hand-side of Eq. (A4)
 1148 then simplifies to $r_c/(r_c + B/2)$. The second term, $\eta|_{r_{thal}}$, is anticipated to be somewhat deeper
 1149 relative to the floodplain surface than the reference channel depth (H_0) due to scour at the outside
 1150 of the bend; however, the possibility exists that under certain conditions, the numerical
 1151 simulation may yield a very wide, shallow channel. The simplest approximation to allow for
 1152 either deepening or shallowing relative to the reference condition is to set $\eta|_{r_{thal}} = -H_0$, in which
 1153 the floodplain surface serves as the vertical datum. The above approximations are expressed in
 1154 Eqs. (A5) and (A6).

$$1155 \quad r_{thal} \approx r_{out} = r_c + \frac{B}{2} \quad (A5)$$

$$1156 \quad \eta|_{r_{thal}} \approx -H_0 \quad (A6)$$

1157 The third unknown term in Eq. (A4), $\eta|_{r_{in}}$, can be approximated more realistically. Assuming the
 1158 dominant hydrodynamic forces are associated with the downstream components of gravity and
 1159 bed shear stress, the maximum possible elevation of $\eta|_{r_{in}}$ at which sediment can be transported
 1160 and deposited is approximated as follows:

$$1161 \quad \tau^*|_{r_{in}} = \tau_{c0}^* \quad (A7)$$

$$1162 \quad \tau^*|_{r_{in}} \approx \frac{h|_{r_{in}} S|_{r_{in}}}{R_s D_{50}} = \frac{h|_{r_{in}} S_c r_c}{R_s D_{50} r_{in}} \quad (A8)$$

$$1163 \quad \eta|_{r_{in}} \approx -h|_{r_{in}} \quad (A9)$$

1164 Combining Eqs. (A7) through (A9) yields:

$$1165 \quad \eta|_{r_{in}} \approx -\tau_{c0}^* \frac{R_s D_{50} r_{in}}{S_c r_c} \quad (A10)$$

1166 Substituting Eqs. (A5), (A6), and (A10) into Eq. (A4) yields:

$$1167 \quad \eta|_{r_{out}} = -H_0 + \left(\frac{r_c}{r_c + \frac{B}{2}} \right) \left(H_0 - \tau_{c0}^* \frac{R_s D_{50} r_{in}}{S_c r_c} \right) \quad (A11)$$

1168 in which the floodplain surface is the vertical datum. Equation (A11) yields reasonable values for
 1169 $\eta|_{r_{out}}$ with viable steady-state migration for most conditions evaluated, but values were slightly too
 1170 high on the bank to prevent aggradation to a static channel for all conditions. Noting that Eq.
 1171 (A8) may overestimate $\tau^*|_{r_{in}}$ due to momentum extraction at the side boundary not accounted for
 1172 in the equation and that a transverse slope may warrant a somewhat greater value than τ_{c0}^* in Eq.
 1173 (A7), a coefficient was added to the right-hand-side of Eq. (A8). Through trial and error, the
 1174 coefficient 1.2 yielded a steady-state solution over all the evaluated conditions. The modified
 1175 version of Eq. (A11) used to set $\eta|_{r_{out}}$ in the simulations is thus:

$$1176 \quad \eta|_{r_{out}} = -H_0 + \left(\frac{r_c}{r_c + \frac{B}{2}} \right) \left(H_0 - 1.2 \tau_{c0}^* \frac{R_s D_{50} r_{in}}{S_c r_c} \right) \quad (A12)$$

1177 **Appendix B: Details of Hydrodynamic Treatment**

1178 The velocity vector is represented by three components u , v , w , which represent the streamwise,
 1179 radial, and vertical components, respectively. In the near-bank region where the w component of
 1180 velocity is non-negligible, a three-dimensional hydrodynamic model accounting for non-
 1181 hydrostatic pressure would clearly be the most accurate treatment; however, it comes at a
 1182 significant computational expense. Most morphodynamics models use depth-averaged
 1183 hydrodynamics, with the assumption of hydrostatic pressure. In the modified cylindrical
 1184 coordinates for steady, uniform bend flow with hydrostatic pressure assumption, the mass and
 1185 momentum (s and r) conservation equations before depth-averaging are as follows:

$$1186 \quad \frac{1}{r} \frac{\partial(vr)}{\partial r} + \frac{\partial w}{\partial z} = 0 \quad (B1)$$

$$1187 \quad -g \frac{\partial \xi}{\partial s} + \frac{\partial}{\partial r} \left(\frac{(v_T + v)}{r} \frac{\partial(ur)}{\partial r} \right) + \frac{\partial}{\partial z} \left((v_T + v) \frac{\partial u}{\partial z} \right) - v \frac{\partial u}{\partial r} - w \frac{\partial u}{\partial z} - \frac{uv}{r} = 0 \quad (B2)$$

$$1188 \quad -g \frac{\partial \xi}{\partial r} + \frac{\partial}{\partial r} \left(\frac{(v_T + \nu) \partial(vr)}{r} \right) + \frac{\partial}{\partial z} \left((v_T + \nu) \frac{\partial v}{\partial z} \right) - v \frac{\partial v}{\partial r} - w \frac{\partial v}{\partial z} + \frac{u^2}{r} = 0 \quad (B3)$$

1189 where g is the gravitational acceleration constant; v_T is the turbulent eddy viscosity; and ν is the
 1190 molecular kinematic viscosity of water. The w momentum equation, not shown, simplifies to a
 1191 linear relation between pressure and depth below the free surface.

1192 Treatment of the r -momentum equation, Eq. (B3), is based on van Bendegom (1947) and
 1193 Rozovskii (1961) as described in Jansen et al. (1979; Ch. 2.2.8 therein). Such analyses are based
 1194 on fully-developed bend flow in the region away from the bank, which allows usage of the
 1195 hydrostatic pressure assumption and neglecting all terms in Eq. (B3) except the following: the
 1196 first term (pressure gradient), the second term (r - shear on z - faces), and the last term (centripetal
 1197 acceleration). In the near-bank region, where v and w will be of the same order of magnitude, the
 1198 error introduced through this simplification must be considered significant; however, in the
 1199 present state of knowledge, a tractable method to integrate the equations to yield suitably simple
 1200 formulations for use in morphodynamics models does not exist.

1201 **References**

- 1202 Abad, J. D., & García, M. H. (2006). RVR Meander: A toolbox for re-meandering of
 1203 channelized streams. *Computers & Geosciences*, 32(1), 92-101.
- 1204 Ariathurai, C. R. (1974). *A finite element model for sediment transport in estuaries*, (Doctoral
 1205 dissertation). University of California, Davis.
- 1206 Asahi, K., Shimizu, Y., Nelson, J., & Parker, G. (2013). Numerical simulation of river
 1207 meandering with self-evolving banks. *Journal of Geophysical Research: Earth Surface*,
 1208 118(4), 2208-2229.
- 1209 Blanckaert, K. (2011). Hydrodynamic processes in sharp meander bends and their morphological
 1210 implications. *Journal of Geophysical Research: Earth Surface*, 116(F1).
- 1211 Brooks, N. H., & Shukry, A. (1963). Discussion of “Boundary Shear Stresses in Curved
 1212 Trapezoidal Channels”. *Journal of the Hydraulics Division*, 89(3), 327-345.
- 1213 Darby, S. E., Rinaldi, M., & Dapporto, S. (2007). Coupled simulations of fluvial erosion and
 1214 mass wasting for cohesive river banks. *Journal of Geophysical Research: Earth Surface*,
 1215 112(F3).

- 1216 Diplas, P. (1990). Characteristics of self-formed straight channels. *Journal of Hydraulic*
1217 *Engineering*, 116(5), 707-728.
- 1218 Duan, J. G., & Julien, P. Y. (2005). Numerical simulation of the inception of channel
1219 meandering. *Earth Surface Processes and Landforms*, 30(9), 1093-1110.
- 1220 Duan, J. G., Wang, S. S., & Jia, Y. (2001). The applications of the enhanced CCHE2D model to
1221 study the alluvial channel migration processes. *Journal of Hydraulic Research*, 39(5), 469-
1222 480.
- 1223 Engelund, F. (1974). Flow and bed topography in channel bends. *Journal of the Hydraulics*
1224 *Division*, 100(11), 1631-1648.
- 1225 Eke, E., Parker, G., & Shimizu, Y. (2014). Numerical modeling of erosional and depositional
1226 bank processes in migrating river bends with self-formed width: Morphodynamics of bar
1227 push and bank pull. *Journal of Geophysical Research: Earth Surface*, 119(7), 1455-1483.
- 1228 Fernandez Luque, R., & Van Beek, R. (1976). Erosion and transport of bed-load sediment.
1229 *Journal of hydraulic research*, 14(2), 127-144.
- 1230 Friedkin, J. F. (1945). *A laboratory study of the meandering of alluvial rivers*. U.S. Waterways
1231 Experiment Station, Vicksburg, MS.
- 1232 Glover, R. E., & Florey, Q. L. (1951). *Stable Channel Profiles* (Hydraulics Laboratory Report
1233 no. 325). Denver, CO: U.S. Bureau of Reclamation.
- 1234 Gough, S. C. (1994). *Geomorphic reconnaissance and draft management strategy for the*
1235 *Mackinaw River ecosystem, Illinois*. The Nature Conservancy, Peoria, Illinois Field Office.
- 1236 Hackney, C., Best, J., Leyland, J., Darby, S. E., Parsons, D., Aalto, R., & Nicholas, A. (2015).
1237 Modulation of outer bank erosion by slump blocks: Disentangling the protective and
1238 destructive role of failed material on the three-dimensional flow structure. *Geophysical*
1239 *Research Letters*, 42(24), 10-663.
- 1240 Hasegawa, K. (1989). Universal bank erosion coefficient for meandering rivers. *Journal of*
1241 *Hydraulic Engineering*, 115(6), 744-765.
- 1242 Ikeda, S. (1981). Self-formed straight channels in sandy beds. *Journal of the Hydraulics*
1243 *Division*, 107(4), 389-406.
- 1244 Ikeda, S., & Nishimura, T. (1986). Flow and bed profile in meandering sand-silt rivers. *Journal*
1245 *of Hydraulic Engineering*, 112(7), 562-579.

- 1246 Ikeda, S., Parker, G., & Sawai, K. (1981). Bend theory of river meanders. Part 1. Linear
1247 development. *Journal of Fluid Mechanics*, 112, 363-377.
- 1248 Ikeda, S., Parker, G., & Kimura, Y. (1988). Stable width and depth of straight gravel rivers with
1249 heterogeneous bed materials. *Water Resources Research*, 24(5), 713-722.
- 1250 Jansen, P., Van Bendegom, L., Van den Berg, J., De Vries, M., & Zanen, A. (1979). *Principles*
1251 *of river engineering: the non-tidal alluvial river*. Pitman Publishing, London.
- 1252 Johnstone, P. D. (2003). Surficial geology of Tazewell County, Illinois. *Open File Series 2003-*
1253 *06a*. Illinois State Geological Survey, Champaign, Illinois.
- 1254 Khodashenas, S. R., & Paquier, A. (1999). A geometrical method for computing the distribution
1255 of boundary shear stress across irregular straight open channels. *Journal of Hydraulic*
1256 *Research*, 37(3), 381-388.
- 1257 Kikkawa, H., Ikeda, S. & Kitagawa, A. (1976). Flow and bed topography in curved open
1258 channels. *Journal of the Hydraulics Division*, 102(9), 1327-1342.
- 1259 Klavon, K., Fox, G., Guertault, L., Langendoen, E., Enlow, H., Miller, R., & Khanal, A. (2017).
1260 Evaluating a process-based model for use in streambank stabilization: Insights on the Bank
1261 Stability and Toe Erosion Model (BSTEM). *Earth Surface Processes and Landforms*, 42(1),
1262 191-213.
- 1263 Kovacs, A., & Parker, G. (1994). A new vectorial bedload formulation and its application to the
1264 time evolution of straight river channels. *Journal of Fluid Mechanics*, 267, 153-183.
- 1265 Lane, E. W. (1955). Design of stable channels. *Transactions of the American Society of Civil*
1266 *Engineers*, 120(1), 1234-1260.
- 1267 Langendoen, E. J., & Simon, A. (2008). Modeling the evolution of incised streams. II:
1268 Streambank erosion. *Journal of Hydraulic Engineering*, 134(7), 905-915.
- 1269 Langendoen, E. J., Mendoza, A., Abad, J. D., Tassi, P., Wang, D., Ata, R., et al. (2016).
1270 Improved numerical modeling of morphodynamics of rivers with steep banks. *Advances in*
1271 *Water Resources*, 93, 4-14.
- 1272 Mackin, J. H. (1948). Concept of the graded river. *Geological Society of America Bulletin*, 59(5),
1273 463-512.
- 1274 McAnally, W. H., & Mehta, A. J. (2001). Preface. In W. H. McAnally & A. J. Mehta (Eds.),
1275 *Coastal and estuarine fine sediment processes, Proceedings in Marine Science* (Vol. 3, pp. v-
1276 vii). Amsterdam: Elsevier.

- 1277 Millar, R. G., & Quick, M. C. (1993). Effect of bank stability on geometry of gravel rivers.
1278 *Journal of Hydraulic Engineering*, 119(12), 1343-1363.
- 1279 Mosselman, E. (1998). Morphological modelling of rivers with erodible banks. *Hydrological*
1280 *Processes*, 12(8), 1357-1370.
- 1281 Motta, D., Abad, J. D., Langendoen, E. J., & García, M. H. (2012). A simplified 2D model for
1282 meander migration with physically-based bank evolution. *Geomorphology*, 163, 10-25.
- 1283 Motta, D., Langendoen, E. J., Abad, J. D., & García, M. H. (2014). Modification of meander
1284 migration by bank failures. *Journal of Geophysical Research: Earth Surface*, 119(5), 1026-
1285 1042.
- 1286 Nanson, G. C. (1980). Point bar and floodplain formation of the meandering Beatton River,
1287 northeastern British Columbia, Canada. *Sedimentology*, 27(1), 3-29.
- 1288 Osman, A. M., & Thorne, C. R. (1988). Riverbank stability analysis. I: Theory. *Journal of*
1289 *Hydraulic Engineering*, 114(2), 134-150.
- 1290 Parker, G. (1978). Self-formed straight rivers with equilibrium banks and mobile bed, Part 2, The
1291 gravel river. *Journal of Fluid Mechanics*, 89(1), 127-146.
- 1292 Parker, G. (1984). Discussion of "Lateral bed load transport on side slopes" by Syunsuke Ikeda
1293 (November, 1982). *Journal of Hydraulic Engineering*, 110(2), 197-199.
- 1294 Parker, G., & Andrews, E. D. (1985). Sorting of bed load sediment by flow in meander bends.
1295 *Water Resources Research*, 21(9), 1361-1373.
- 1296 Parker, G., Shimizu, Y., Wilkerson, G. V., Eke, E. C., Abad, J. D., Lauer, J. W., et al. (2011). A
1297 new framework for modeling the migration of meandering rivers. *Earth Surface Processes*
1298 *and Landforms*, 36(1), 70-86.
- 1299 Pizzuto, J. E. (1990). Numerical simulation of gravel river widening. *Water Resources Research*,
1300 26(9), 1971-1980.
- 1301 Rinaldi, M., & Darby, S. E. (2008). Modelling river-bank-erosion processes and mass failure
1302 mechanisms: Progress towards fully coupled simulations. In H. Habersack, H. Piegay, M.
1303 Rinaldi (Eds.), *Gravel-Bed Rivers VI: From Process Understanding to River Restoration* (pp.
1304 213-239). Amsterdam: Elsevier.
- 1305 Rinaldi, M., & Nardi, L. (2013). Modeling interactions between riverbank hydrology and mass
1306 failures. *Journal of Hydrologic Engineering*, 18(10), 1231-1240.

- 1307 Rinaldi, M., Mengoni, B., Luppi, L., Darby, S. E., & Mosselman, E. (2008). Numerical
1308 simulation of hydrodynamics and bank erosion in a river bend. *Water Resources Research*,
1309 44(9).
- 1310 Rozovskii, I. L. (1961). *Flow of water in bends of open channels*: Israel Program for Scientific
1311 Translation. Jerusalem, 233p.
- 1312 Schumm, S. A., & Khan, H. R. (1972). Experimental study of channel patterns. *Geological*
1313 *Society of America Bulletin*, 83(6), 1755-1770.
- 1314 Seminara, G., Solari, L., & Parker, G. (2002). Bed load at low Shields stress on arbitrarily
1315 sloping beds: Failure of the Bagnold hypothesis. *Water Resources Research*, 38(11), 31-1.
- 1316 Shimizu, Y., Takebayashi, H., Inoue, T., Hamaki, M., Iwasaki, T., & Nabi, M. (2014). *Nays2DH*
1317 *Solver Manual*. iRIC Project, Hokkaido, Japan.
- 1318 Simon, A., Curini, A., Darby, S. E., & Langendoen, E. J. (2000). Bank and near-bank processes
1319 in an incised channel. *Geomorphology*, 35(3-4), 193-217.
- 1320 Siviglia, A., & Crosato, A. (2016). Numerical modelling of river morphodynamics: Latest
1321 developments and remaining challenges. *Advances in Water Resources*, 93(Part A), 1-3.
- 1322 Stecca, G., Measures, R., & Hicks, D. M. (2017). A framework for the analysis of noncohesive
1323 bank erosion algorithms in morphodynamic modeling. *Water Resources Research*, 53(8),
1324 6663-6686.
- 1325 Thorne, C. R. (1982). Processes and mechanisms of river bank erosion. In R. D. Hey, J. C.
1326 Bathurst, C. R. Thorne (Eds.), *Gravel-bed Rivers* (pp. 227–271). Chichester: Wiley.
- 1327 Thorne, C. R., & Tovey, N. K. (1981). Stability of composite river banks. *Earth Surface*
1328 *Processes and Landforms*, 6(5), 469-484.
- 1329 Thorne, C. R., Alonso, C., Borah, D., Darby, S., Diplas, P., Julien, P., et al. (1998). River width
1330 adjustment. I: Processes and mechanisms. *Journal of Hydraulic Engineering*, 124(9), 881-
1331 902.
- 1332 Tsujimoto, T. (1999). Fluvial processes in streams with vegetation. *Journal of Hydraulic*
1333 *Research*, 37(6), 789-803.
- 1334 van Bendegom, L. (1947). Some considerations on river morphology and river improvement. *De*
1335 *Ingenieur*, 59(4), 1-11 (in Dutch; English transl.: Nat. Res. Counc. Canada, Technical
1336 Translation 1054, 1963).

- 1337 Vanoni, V. A., (Ed.). (1975). *Sedimentation Engineering*, ASCE Manual and Reports on
1338 Engineering-Practice, 54, New York.
- 1339 Waterman, D. M. (2017). *Non-cohesive bank migration in meandering rivers and bank accretion*
1340 *in weakly braided rivers* (Doctoral dissertation, University of Illinois at Urbana-Champaign).
- 1341 Waterman, D. M., & García, M. H. (2016). Concave-upward composite river bank profile shape
1342 at migrating meander bends. In *International Conference on Fluvial Hydraulics, RIVER*
1343 *FLOW 2016* (pp. 1098-1105). CRC Press/Balkema.
- 1344 Waterman, D. M., & García, M. H. (2019). Nonlinear Bedload Transport Trajectory Angle
1345 Expressed in a Traditional Form: Derivation and Application. *Journal of Hydraulic*
1346 *Engineering*, 145(8), 04019028.
- 1347 Wiberg, P. L., & Smith, J. D. (1987). Calculations of the critical shear stress for motion of
1348 uniform and heterogeneous sediments. *Water Resources Research*, 23(8), 1471-1480.